


Numerical study of the transcritical shock-droplet interaction

Bradley Boyd * and Dorrin Jarrahbashi*J. Mike Walker '66 Mechanical Engineering Department, Texas A&M University,
College Station, Texas 77843, USA*

(Received 3 May 2021; accepted 25 October 2021; published 15 November 2021)

Transcritical shock-droplet interactions (TSDIs) occur in a spectrum of high-speed propulsion systems involving liquid fuel injection. “Transcritical” behavior refers to a condition at which the combustion chamber pressure nears the critical pressure of the fuel-air mixture and, by increasing the temperature, a transition from liquidlike to gaslike state is observed. Our understanding of TSDI is significantly less developed than its gas-phase (ideal-gas or supercritical) or liquid-phase (subcritical) counterparts, which are referred to as shock-bubble interactions (SBIs) and shock-droplet interactions (SDIs), respectively. In this paper, we investigate the interaction of a shockwave with an *n*-dodecane droplet at supercritical pressures. A fully conservative diffuse-interface framework coupled with the Peng-Robinson equation of state is developed to accurately determine the state of the fluid and the resulting interfacial instabilities as the shock propagates through the droplet. The influence of varying the initial temperature of the fuel, the ambient pressure, and the shockwave strength on the shock structure and the droplet morphological deformation is delineated. The dynamics of the TSDI cases are then compared to the subcritical SDI and supercritical or ideal-gas SBI counterparts. It is shown that, depending on the preshock temperature and pressure, the TSDIs exhibit some common features observed in classical cases of SDIs and SBIs, bridging the gap between the sub- and supercritical problems.

DOI: [10.1103/PhysRevFluids.6.113601](https://doi.org/10.1103/PhysRevFluids.6.113601)

I. INTRODUCTION

The design of current and future energy conversion systems is shifting toward supercritical pressures to enable performance gain and lighter and more reliable systems for space [1–7], aviation [8–14], ground transportation [15–20], and power generation [21]. Shock-droplet interactions (SDIs) occur in a spectrum of high-speed propulsion systems involving liquid fuels including ramjets and scramjets [22,23]. In applications such as high-speed diesel injection, shock waves may be induced and interact with the fuel spray [24]. Shock-bubble interactions (SBIs) and SDIs have been the subject of many studies over the past decades [25–37]. The seminal work of Haas and Sturtevant [38] revealed very complex phenomena occurring during shock interaction with helium and R22 refrigerant bubbles. Later, these cases were numerically modeled highlighting the features of the shock-bubble interactions [39]. Since then, additional cases have been considered, including the bubble composition of SF6 and krypton [40–54]. However, these studies are all conducted at atmospheric pressure and room temperature where the fluids are in a gaseous state. Understanding the disintegration of droplets impacted by shocks at supercritical conditions is relevant to liquid-fueled scramjet engines during low hypersonic, i.e., start-up operations, and will inform the mixing and combustion behavior of liquid fuel sprays in a spectrum of supercritical and high-speed propulsion systems, particularly in hypersonic flights [22,23,55,56]. Although a

*bradley.boyd@tamu.edu

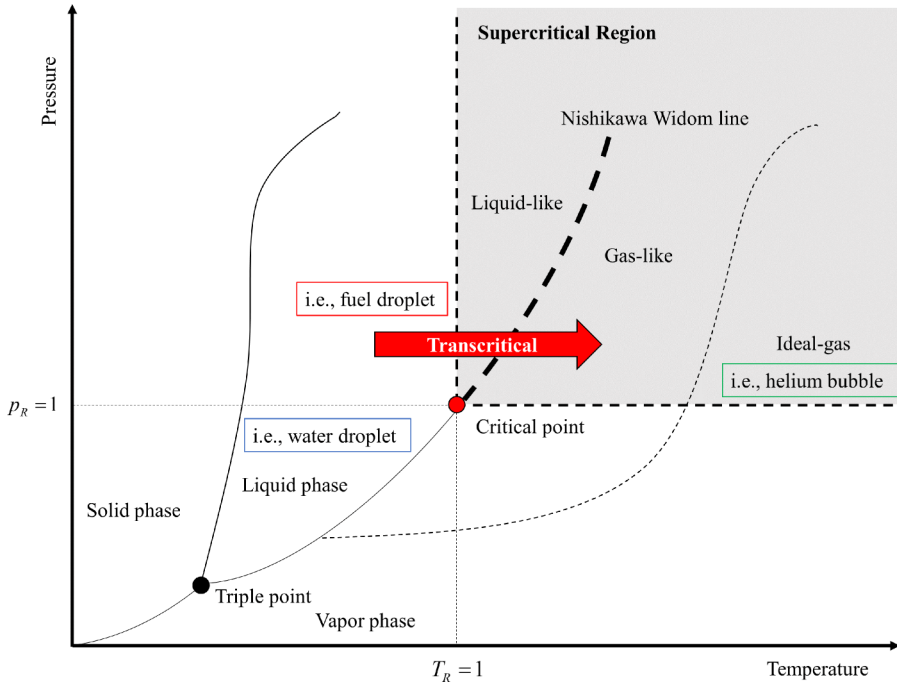


FIG. 1. Representative state diagram showing the “transcritical” state of an injected fuel. The diagram is in terms of reduced pressure ($p_r = p/p_c$) and temperature ($T_r = T/T_c$). In the case of fuel injection into a combustion chamber, the fuel is injected at supercritical pressure and mixes with the hot ambient air, increasing the temperature of the fuel. As the fuel is heated, it transitions from a liquidlike to a gaslike supercritical fluid as it crosses the Nishikawa Widom line—this is termed *pseudoboiling* and is an example of a transcritical problem [73,84,85]. The depiction also annotates the classic examples of a subcritical droplet (i.e., water droplet) and ideal gas (i.e., helium bubble).

better understanding of the sub- and supercritical conditions has been obtained by numerical and experimental efforts, there is still a critical *gap in the knowledge* on the transcritical conditions where the transition from liquidlike to gaslike behavior occurs by crossing the pseudoboiling line [57,58].

At transcritical conditions, both subcritical (two-phase) and supercritical (diffusion-controlled) behaviors might emerge [18,19]. Classical transcritical cases involve fuel injected at a pressure above the critical pressure (the reduced pressure $p_r = p/p_c > 1$). In the case of fuel injection into a combustion chamber, the fuel with a temperature initially below the critical temperature (the reduced temperature $T_r = T/T_c < 1$) is injected at supercritical pressure, mixes with the hot ambient air, and increases the temperature of the fuel. As the fuel is heated, it transitions from liquidlike to gaslike supercritical fluid and crosses the Nishikawa Widom line (termed *pseudoboiling*) as shown in Fig. 1. At temperatures above the critical temperature, the fuel will behave as an ideal gas when the compressibility factor is equal to unity.

To date, studies of supercritical droplets have focused on low-speed convective environments where droplet vaporization is significantly influenced by viscous effects and heat conduction. For example, multiple studies have investigated the behavior of liquid oxygen droplets in a supercritical hydrogen environment at supercritical conditions [59–62]. A more recent study by Crua *et al.* [63] experimentally investigated the convection of hydrocarbon fuel droplets, including *n*-dodecane, reporting cases of sustained surface tension. All of these supercritical droplet studies report the formation of a “crescent shape” [64], “backward-facing bag” [8,63], or “skirt” [62] droplet at later times. These studies, however, lacked insight into the droplet interaction with a shock wave or

high-speed flow, where the influence of the diffuse effects (i.e., viscosity and thermal diffusion) and the surface tension force is expected to be negligible, especially in the early stages of the droplet development.

For the design of high-pressure and high-speed propulsion systems, it is of great interest to understand the behavior of fuel droplets impacted by shockwaves at pressures above the critical pressure. The lack of knowledge on multiphase shock-driven instabilities due to the dearth of detailed experimental data at such high pressure (and temperature) is the main motivation behind this computational study that focuses on the shock interaction with fuel droplets at near-critical conditions.

There are many reports on simulations of SDI using sharp-interface and diffuse-interface approaches at subcritical conditions [32,65–69]. However, there are only two reports that simulate the fuel droplet-shock interaction at transcritical conditions [70,71]. To the authors' knowledge, the underlying physics behind this problem has not been previously investigated. In our previous work [71], we briefly considered the shock interaction with an *n*-dodecane droplet at near-critical conditions. Here, we consider the shock interaction of droplets above the critical pressure (i.e., the reduced pressure $p_r > 1$) at varying temperatures on either side of the Widom line, i.e., from subcritical to supercritical temperatures. It is important to note that the physics associated with a fluid near the critical point is significantly different from conventional liquid droplets or ideal-gas bubbles. For the shock-bubble interaction problem, the sphere of fluid is referred to as a *bubble* because it is in a gaseous state, typically an ideal gas, e.g., in a helium gas bubble indicated in Fig. 1. The term *droplet* is typically associated with a liquid sphere with significant surface tension effects, e.g., the water droplet marked in Fig. 1. However, this differentiation breaks down for a supercritical fluid where gaslike and liquidlike properties better represent the state of the fluid [72] (Fig. 1). Although at supercritical conditions surface tension is typically neglected [19,73–83], we use the term *droplet* for the fuel sphere at all tested conditions in this paper. The main research questions to be answered in this paper include (1) how the interfacial hydrodynamic instability mechanisms and mixing behavior change during the transition between sub- and supercritical regimes and (2) how the droplet disintegration behavior at transcritical conditions is related to the classical SDI and SBI. Finally, how does the variation in Mach number, pressure, and temperature affect the physics of the transcritical SDI (TSDI)?

In the present paper, we first describe the numerical methodology (Sec. II). Finally, we investigate the shock interaction with the supercritical fuel sphere (Sec. III) by analyzing the physics of the interaction including shock characteristics, instability development, droplet deformation, and induced vorticity. The results consider the influence of varying temperature, pressure, and shock strength on the TSDI.

II. METHODOLOGY

A. Governing equations

We consider a compressible, inviscid, multiphase model. The governing equations for a diffuse-interface two-species system, including the conservation of mass, species, momentum, and total energy, are given below:

$$\frac{\partial \rho}{\partial t} + \nabla \cdot (\rho \mathbf{u}) = 0, \quad (1)$$

$$\frac{\partial (\rho Y_D)}{\partial t} + \nabla \cdot (\rho \mathbf{u} Y_D) = 0, \quad (2)$$

$$\frac{\partial (\rho \mathbf{u})}{\partial t} + \nabla \cdot (\rho \mathbf{u} \otimes \mathbf{u} + p \mathbf{I}) = \mathbf{0}, \quad (3)$$

$$\frac{\partial E}{\partial t} + \nabla \cdot [\mathbf{u}(E + p)] = 0, \quad (4)$$

where Y_D is the mass fraction of the bubble or droplet fluid species, ρ is the density, \mathbf{u} is the velocity vector, p is the pressure, E is the total energy $E = \rho(e + |\mathbf{u}|^2/2)$, e is the internal energy, and \mathbf{I} is the identity matrix. The mass fraction of the second species of the two-component system (D and S representing the droplet or bubble and the surrounding fluids, respectively) is given by the mixture rule $Y_S = 1 - Y_D$. The system of equations, Eqs. (1)–(4), is closed using the Peng-Robinson equation of state (PR-EoS) [86] as follows:

$$p = \frac{R_U T}{V_m - b} - \frac{a}{V_m^2 + 2bV_m - b^2}, \quad (5)$$

where T is the temperature, R_U is the universal gas constant, V_m is the molar volume $V_m = M/\rho$, M is the molar mass, and a and b are coefficients that depend on the state and composition of the fluid. The PR-EoS is modified [71] to approximate the state of the fluid in the vapor dome region to increase the robustness of the numerical method. This is important at the interface where the binary mixture may result in phase separation in small regions. Because these regions are small, the approximation has an insignificant influence on the shock transmission across the fluid interface. The parameters for the NASA polynomials that are used to determine the internal energy, enthalpy, and entropy were adopted from Ref. [87].

The present model neglects surface tension and the diffuse terms including molecular diffusion, viscous effects, thermal conduction, and chemical reactions. Surface tension is typically neglected in transcritical flows [19,73–83] as the surface tension coefficient drops dramatically at the critical point. The viscous effects and thermal conduction may be important for longer duration simulations or low-speed cases; however, we found that for the cases considered in the present paper the thermal and viscous terms are insignificant. For the sake of brevity, we did not include the cases including thermal and viscous terms. The interested reader is referred to the work of Ma *et al.* [73,88]. Similarly, the molecular diffusion is expected to be negligible as it has been shown in earlier studies [88] that the diffuse effects are typically less than the numerical diffusion of the numerical model and, thus, no additional insight is gained by the inclusion of the diffuse terms.

We consider the TSDI problem in idealized two-dimensional (2D) axisymmetric cylindrical coordinates to reduce the high computational costs inherited in the three-dimensional model. In Chen *et al.* [25], it was stated that interfacial instabilities that arise in cylindrical coordinates are less physical than in 2D Cartesian coordinates. However, we simulated the cases in both 2D Cartesian coordinates (shock-column interactions) and 2D cylindrical coordinates, and the comparison showed qualitatively insignificant changes to the shock-droplet interaction. We adopted the 2D axisymmetric coordinates for modeling the early stages of the droplet breakup in this paper.

This paper uses DIMP-CFD code, which is an in-house, density-based, finite volume solver in C++ parallelized using domain decomposition and the message passing interface (MPI), which is presented in Ref. [71]. In the same study, we introduced a hybrid (HY) numerical method, which hybridizes the fully-conservative (FC) procedure with the double-flux (DF) method [71]. HY method is chosen for this paper as our earlier study proved that the HY method can significantly reduce the magnitude of pressure oscillation while limiting the loss of energy conservation when a shock impacts the nitrogen–*n*-dodecane interface. To avoid the interaction of the characteristic fields and increase the robustness and stability of the solver, we reconstruct the primitive variables in the characteristic space, i.e., characteristicwise (CW) reconstruction [71,89–92].

The temporal discretization of Eqs. (1)–(4) uses the third-order total-variation-diminishing Runge-Kutta scheme (RK3-TVD) [93] with a CFL equal to 0.8. The Harten–Lax–van Leer-contact (HLLC) approximate Riemann flux is used to determine the Godunov flux at the cell interfaces [89,94,95]. Additionally, we make use of a maximum-principle-satisfying and positivity-preserving flux limiter to help ensure the boundness of the mass fraction and the positivity of density and pressure [94–96].

Weighted essentially non-oscillatory (WENO)5-CW reconstruction is performed in the axisymmetric cylindrical coordinates– r, z (see Appendix C of Ref. [97] for more details). We also apply the

artificial interface thickening method as discussed in our earlier study [71] to the initial condition of the droplet interface in axisymmetric cylindrical coordinates with $\beta = 2$, where β is the number of finite volume cells the interface is initially smeared over. The interface thickening reduces the jump in properties between cells, reducing pressure oscillations and increasing the numerical stability [71]. Additionally, interface thickening reduces the loss in energy conservation when used with a quasiconservative method like the HY method developed by the authors [71]. Because the droplet is defined on a uniform Cartesian mesh, this interfacial thickening also helps provide the smooth curvature of the initial droplet shape. For the higher strength shock problems presented later in this paper, we further increase the stability by reducing the order of reconstruction to WENO3, and for the Mach 2 shock case we also make use of a minmod flux limiter based on the gradient in the mass fraction [33].

B. Flow visualization

Computational Schlieren images are used to visualize features involving density gradients: material interfaces, shock waves, and rarefaction waves [39,94]. The computational Schlieren images are generated using a shading function (ϕ) defined as

$$\phi = \exp\left(-k \frac{|\Delta\rho|}{|\Delta\rho|_{\max}}\right) \quad (6)$$

where the parameter k is assigned to each fluid component to accentuate the compressible flow features. For the two-component cases presented (i.e., He-N₂ and R22-N₂), we use $k = 120$ for the denser component (i.e., R22) and $k = 600$ for the less dense component (i.e., He) as is suggested in Ref. [39]. For example, in the fuel shock-droplet interaction case, $k = 120$ for the *n*-dodecane droplet, and $k = 600$ for the surrounding nitrogen.

Additionally, vorticity (ω) is visualized by computing the curl of the velocity field: $\nabla \times \mathbf{u}$. The total flow circulation (Γ) is computed by numerical integration of the vorticity in the computational domain. It was suggested in Ref. [48] that in the early stages of a shock-bubble interaction the primary source of vorticity generation is the baroclinic term. The baroclinicity of the flow is the misalignment of the local pressure and density gradients as represented by $\frac{1}{\rho^2}(\nabla\rho \times \nabla p)$. For reference, the vorticity transport equation for an inviscid flow is

$$\frac{D\omega}{Dt} = \overbrace{\frac{1}{\rho^2}(\nabla\rho \times \nabla p)}^{\text{baroclinic term}} + (\omega \cdot \nabla)\mathbf{u} - \omega(\nabla \cdot \mathbf{u}) \quad (7)$$

C. Validation cases: Shock-bubble interaction and shock-droplet interaction

In Appendix B, the model is validated using the two extensively considered SBI problems: (1) the helium bubble case and (2) the R22 refrigerant case. To the authors' knowledge, this is the first time the real-gas equation of state (PR-EoS) has been used to simulate the SBI. The other numerical studies in the literature that use these validation cases typically use the stiffened EoS that simplifies to the ideal-gas law for gases [39,89,97–106]. Additionally, we briefly consider the commonly studied SDI involving a water droplet for comparative purposes (Appendix C).

D. Critical parameters

Here, we introduce the important parameters that change the behavior shock-droplet interaction. The speed of sound (SoS) ratio, that is, the ratio of the SoS between the surrounding fluid and the bubble or droplet fluid, is

$$n = \frac{c_S}{c_D} \quad (8)$$

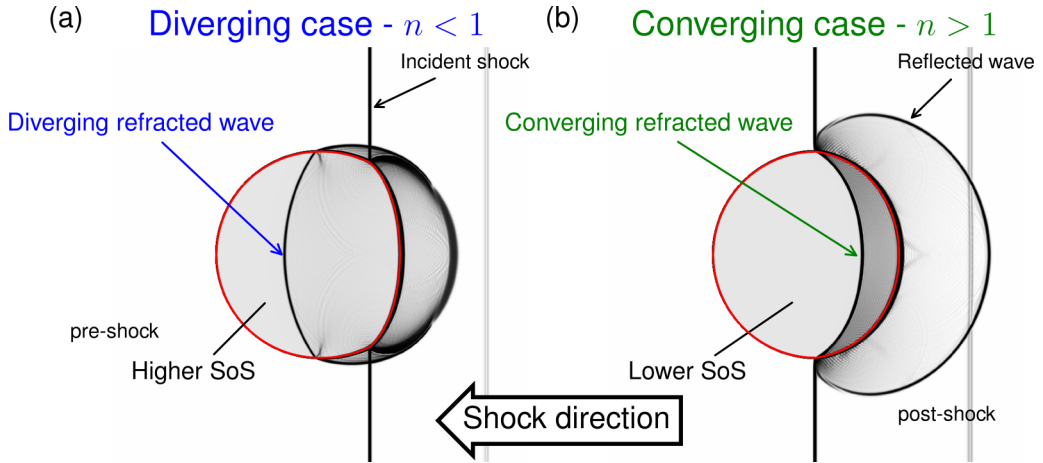


FIG. 2. Schematic of (a) the classic helium diverging case ($n < 1$) and (b) a R22 converging case ($n > 1$). The red contour line shows the material interface at $\alpha_D = 0.95$, where α is the volume fraction.

where c is the SoS, and subscripts D and S denote the bubble or droplet and surrounding fluid, respectively. The ratio of the SoS is an important parameter as it indicates if the refracted shock is going to diverge or converge upon interaction with the bubble or droplet (Fig. 2). If the SoS with the bubble or droplet is greater than the surrounding fluid ($n < 1$), then the refracted shock within the bubble moves ahead of the incident shock [Fig. 2(a)]—a situation that is commonly accepted in the literature as “divergent,” e.g., the helium bubble case [38,92] as is shown in Appendix B. Alternatively, if the SoS within the bubble or droplet is less than the surrounding fluid ($n > 1$), then the refracted shock within the bubble lags behind the incident shockwave and causes the incident shock to focus on the downstream pole of the bubble [Fig. 2(b)] and produce an intense jump in pressure at the focal point as will be shown later. This configuration is referred to as “convergent” and reported for the R22 bubble case [38,92] (see Appendix B).

The next parameter that is associated with the shock-bubble interaction is the acoustic impedance mismatch across the material interface. The acoustic impedance mismatch for a material interface is represented as

$$\delta Z = (\rho c)_D - (\rho c)_S. \quad (9)$$

Acoustic impedance mismatch influences the transition of a shock wave across the material interface. When the incident shock reaches the interface, the shock wave is refracted and a rarefaction or shock wave is reflected [48]. If the impedance mismatch is greater than zero ($\delta Z > 0$), then the reflected wave is a shock wave. Otherwise, if the impedance mismatch is less than zero ($\delta Z < 0$) then the reflected wave is a rarefaction wave. Thus, for the helium case, the reflected wave is a rarefaction wave, and for the R22 case the reflected wave is a shock wave [48]. Once the refracted shock that is passing through the bubble reaches the downstream interface, the opposite impedance mismatch is present. As a result, the internally reflected wave is a shock wave for the helium case and a rarefaction wave for the R22 case.

Another parameter that is typically considered in shock-bubble interaction problems is the Atwood number defined as

$$A = \frac{(\rho_D - \rho_S)}{(\rho_D + \rho_S)}. \quad (10)$$

The Atwood number indicates the effect of the density change between the bubble or droplet and surrounding fluid. It is noted that both the Atwood number (A) and the acoustic impedance mismatch (δZ) are typically used in the literature to classify SBI problems involving divergent or

convergent cases; e.g., $\delta Z > 0$ is reported as convergent, while $\delta Z < 0$ is considered as divergent [46,48,107]. The Atwood number and impedance mismatch are important parameters in classifying shock-bubble interaction problems; however, it has been shown that the diverging and converging behavior can be better defined using the SoS ratio (n) [38,44]. In this paper, we will consider the influence of all the key parameters: A , δZ , and n .

E. Computational experiments

Here, we consider the interaction of a shock wave in a nitrogen environment with a sphere of n -dodecane at supercritical pressure in a liquidlike or gaslike supercritical state to showcase the shock interaction with a transcritical or near-critical droplet (TSDI). In transcritical injection problems, a liquid fuel, initially at subcritical temperatures, is injected into an environment at supercritical pressure and temperatures with respect to the fuel. As the fuel is heated by the ambient environment, its temperature increases from subcritical to supercritical by crossing the pseudoboiling (Widom) line. During this transition, the fuel properties vary from a liquidlike to a gaslike state (Fig. 1). We focus on investigating the shock-droplet interaction state near the Widom line to provide insight into the behavior of the fuel for transcritical scenarios; hence, the term *transcritical shock-droplet interaction*. In this paper, we focus on the n -dodecane as the fuel as n -dodecane has been extensively used as a diesel fuel surrogate in the combustion community [19,73,75,108]. The n -dodecane has a critical temperature of $T_C = 658.1$ K and critical pressure of $p_C = 1.82$ MPa. The nitrogen has a critical temperature of $T_C = 126.2$ K and critical pressure of $p_C = 3.369$ MPa.

The key changes to the n -dodecane and nitrogen system with respect to temperature and pressure are depicted in Fig. 3. The SoS of the nitrogen increases [Fig. 3(a)] and its density decreases [Fig. 3(b)] from 500 and 800 K. The SoS of the n -dodecane drops to a minimum near its critical temperature (658.1 K) and then begins to rise [Fig. 3(a)]. The density of the n -dodecane also drops as the temperature increases past the critical temperature [Fig. 3(b)], coinciding with the transition from a liquidlike to a gaslike supercritical fluid. The transition from liquidlike to gaslike across the Widom line (Fig. 1) and the point of transition is associated with the peak in the specific isobaric heat capacity (c_p) as is evident in Fig. 3.

At the lowest pressure (2 MPa), which is slightly above the critical pressure of n -dodecane ($p_C = 1.82$ MPa), there is an abrupt change in the SoS and density at the pseudoboiling point by crossing the Widom line near the critical pressure [84,85]. The peak in the specific isobaric heat capacity reduces with increasing pressure as shown in Fig. 3(c). Additionally, the minimum SoS of n -dodecane increases with increasing pressure, and as a result the peak in the SoS ratio (n) reduces [Fig. 3(d)]. The change in the SoS near the critical pressure means that, for the preshock pressure of 2 MPa, the SoS ratio reaches a large peak of about $n \approx 6$ when $T \approx T_C = 658.1$ K. As the preshock pressure increases and the changes in properties across the Widom line become less pronounced, we also see a drop in the peak of the SoS ratio. At preshock pressure of 10 MPa, far above the critical pressure, there is no apparent peak in n [Fig. 3(d)]. The importance of n for the TSDI will be discussed next. In Fig. 4, we present all the cases considered in this paper that span a wide range of pressures and temperatures.

F. Computational model

The shock wave travels from right to left, impacting the droplet, where the initial droplet diameter is $D_0 = 5$ [cm]. The nondimensional variables are in terms of D_0 : $z^* = z/D_0$ and $r^* = r/D_0$. The computational domain $\Omega = [-5D_0, 5D_0] \times [0, 6D_0]$ is shown in Fig. 5. The size of the computational domain is sufficiently large so that potential erroneous reflections from the nonreflective boundaries will not interact with the droplet throughout the simulation. The computational domain consists of a uniform mesh from $z^* = -3.2$ to 3.2 and from the axis of symmetry to $r^* = 1$ to increase the computational speed of the simulation where the cell dimensions are $\Delta z^* \approx \Delta r^* \approx 4.6 \times 10^{-3}$. The mesh then grows at a rate of 10% in the z and r directions to the outer boundaries.

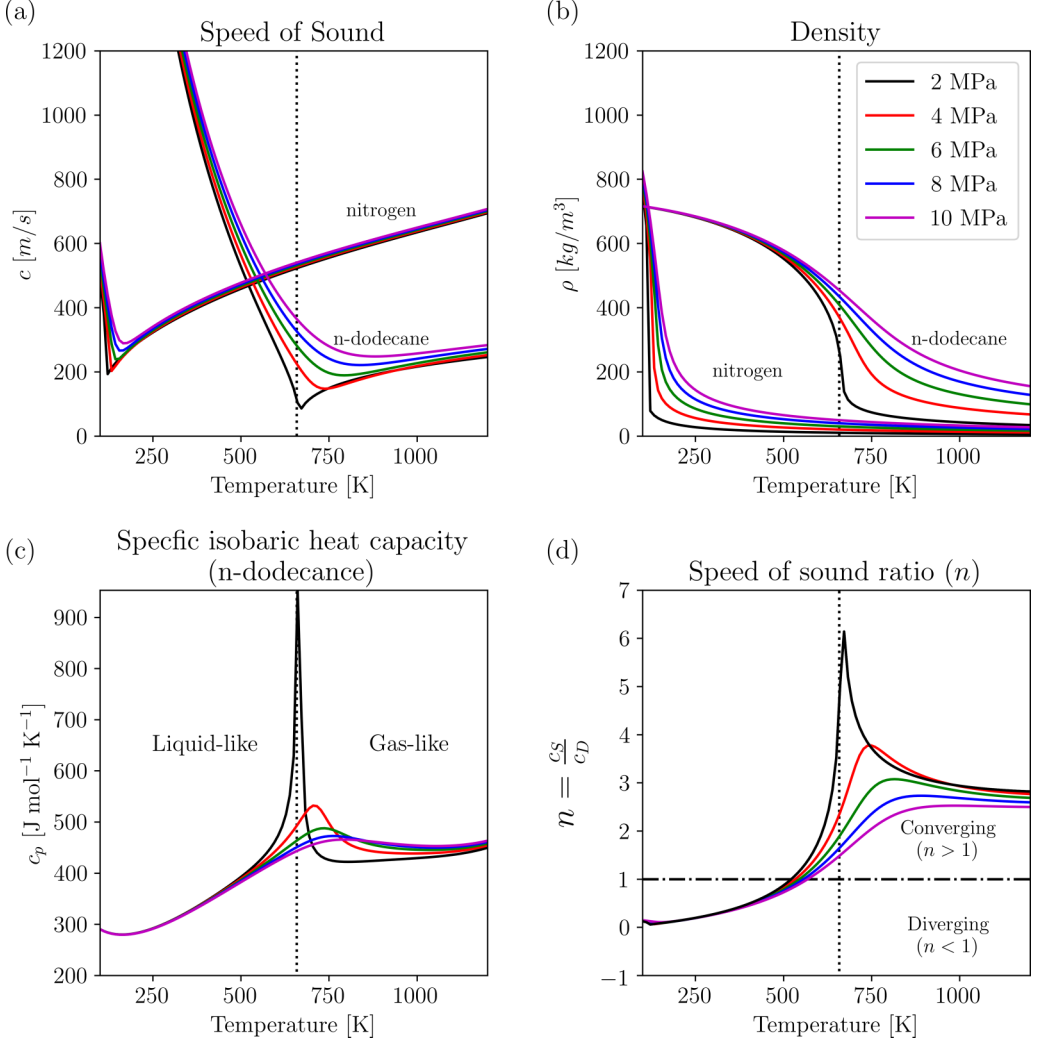
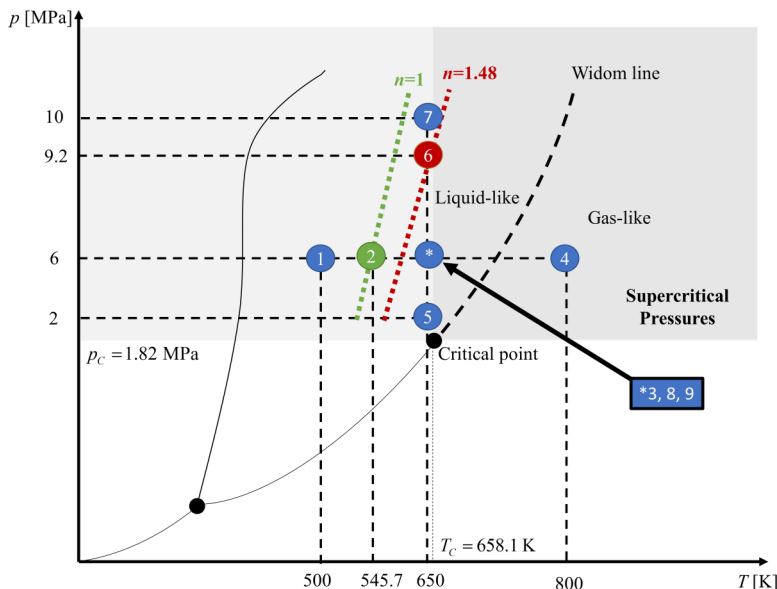


FIG. 3. The change in (a) SoS, (b) density, (c) specific isobaric heat capacity (c_p), and (d) speed of sound ratio (n) with respect to temperature at varying pressures. The vertical dotted line indicates the critical temperature of *n*-dodecane (658.1 K).

Due to the axis of symmetry boundary condition, only the top half of the depicted computational domain is required for the simulation (Fig. 5). A transmissive boundary condition is used at the other boundaries (left, right, and outer boundaries). The initial state of the three regions, (1) preshock, (2) postshock, and (3) the *n*-dodecane droplet, is summarized below:

$$(Y_D, u_z, p, T, \rho) = \begin{cases} (0, 0, p_{\text{PRE}}, T_{\text{PRE}}, \rho_{\text{PRE}}) & \text{preshock} \\ (0, u_{z,\text{POST}}, p_{\text{POST}}, T_{\text{POST}}, \rho_{\text{POST}}) & \text{postshock.} \\ (1, 0, p_{\text{PRE}}, T_{\text{PRE}}, \rho_D) & \text{droplet} \end{cases} \quad (11)$$

Note that u_z is the velocity component in the z direction and the initial velocity in the r direction (u_r) is zero everywhere. The pre- and postshock conditions are outlined in Appendix A (Tables I–III) for all test cases.



Case #	1	2	3	4	5	6	7	8	9
T_{PRE} [K]	500	545.7	650	800	650	650	650	650	650
p_{PRE} [MPa]	6	6	6	6	2	9.2	10	6	6
Mach #	1.2	1.2	1.2	1.2	1.2	1.2	1.2	1.6	2.0
n	0.78	1.0	1.8	3.1	3.5	1.48	1.43	1.8	1.8

FIG. 4. State of the shock-droplet computational cases (1–9) on the n -dodecane phase diagram. The green dotted line indicates the transition line where the speed of sound ratio is $n = 1$ (Sec. III A 1) and the red dotted line indicates where $n = 1.48$, which we later find to be the transition from weak to strong convergent behavior (Sec. III B 1).

The shock wave, which is initially at $z^* = 2$, travels to the left towards the droplet. For this paper, we also make use of the nondimensional breakup time (t^*) derived from the analysis of SDI considering the droplet displacement assuming a constant acceleration due to drag [32,109]:

$$t^* = t \frac{u_{z,POST}}{D_0} \sqrt{\frac{\rho_{POST}}{\rho_D}} \quad (12)$$

where t begins when the shock first impacts the droplet interface at $z^* = 1.5$. This nondimensional breakup time is useful for comparing the instability development of the droplet at later times when the primary shock interactions are complete.

III. RESULTS AND DISCUSSION

First, we show the key features of the TSDI for a special case where $n = 1$. Consider the case where $T_{PRE} = 545.7$ K, $p_{PRE} = 6$ MPa (see Fig. 4), and the incident shock wave is Mach 1.2 (Fig. 6). Note that the time (t) begins when the leftward traveling incident shock reaches the droplet interface [Fig. 6(a)]. Once the shock impacts the droplet, the vertical incident shock above and below the droplet is joined by two shock waves: (1) the refracted shock that lies within the droplet and (2) the reflected shock that is outside the droplet [Fig. 6(b)]. The passage of the refracted shock across the downstream interface results in a transmitted shock and the reflection

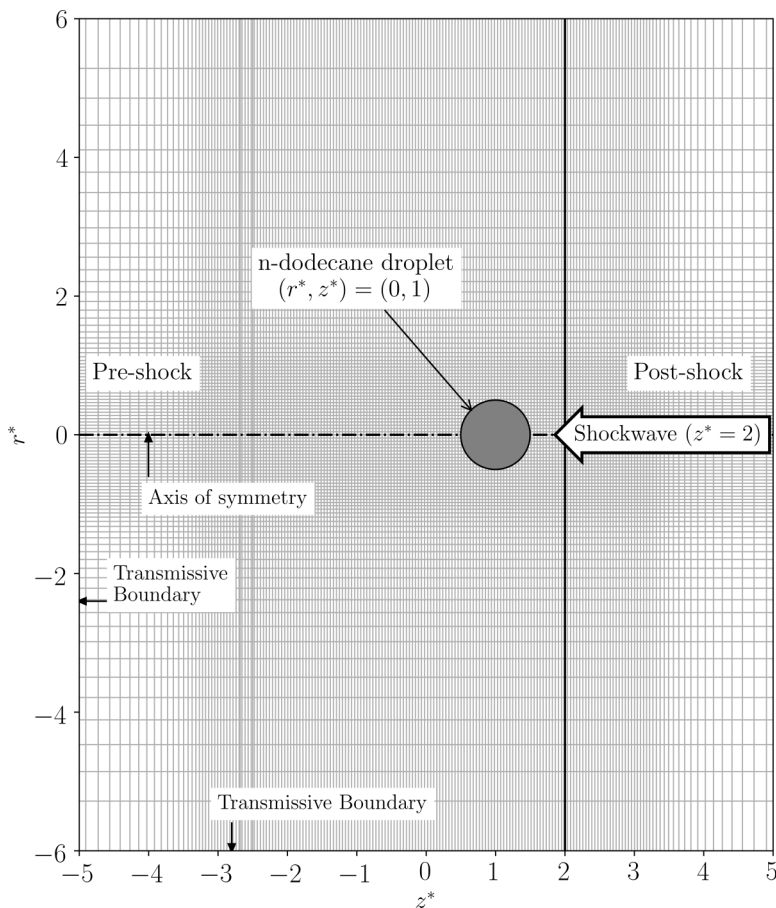


FIG. 5. Depiction of the transcritical shock-droplet case. The depicted cell size is ten times larger than the cell size used in the simulations ($\Delta z^* \approx \Delta r^* \approx 4.6 \times 10^{-3}$). Due to the axis of the symmetry boundary condition, only the top half of the depicted computational domain is required for the simulation.

of a rarefaction wave [Fig. 6(c)]. The acoustic impedance mismatch experienced by the incident shock impacting the droplet is $\delta Z > 0$; however, the internal shock experiences the opposite acoustic impedance mismatch (i.e., $\delta Z < 0$) when interacting with the downstream interface of the droplet. The subsequent acoustic impedance mismatch experienced by the refracted shock results in the internal reflection of a rarefaction wave (see Fig. 3 of Ref. [48] for details). As time progresses, interfacial instabilities begin to grow at the interface between the fuel and the surrounding nitrogen [Fig. 6(d)].

A. Influence of the preshock temperature

We investigate the influence of varying the initial temperature (T_{PRE}) of the droplet and the ambient nitrogen. The cases considered are 500, 545.7, 650, and 800 K (see Fig. 4) and the initial conditions are presented in Table I. Note that 500, 545.7, 650, and 800 K correspond to the reduced temperatures with respect to the critical temperature of *n*-dodecane (T_R), which are approximately 0.76, 0.83, 0.99, and 1.22, respectively.

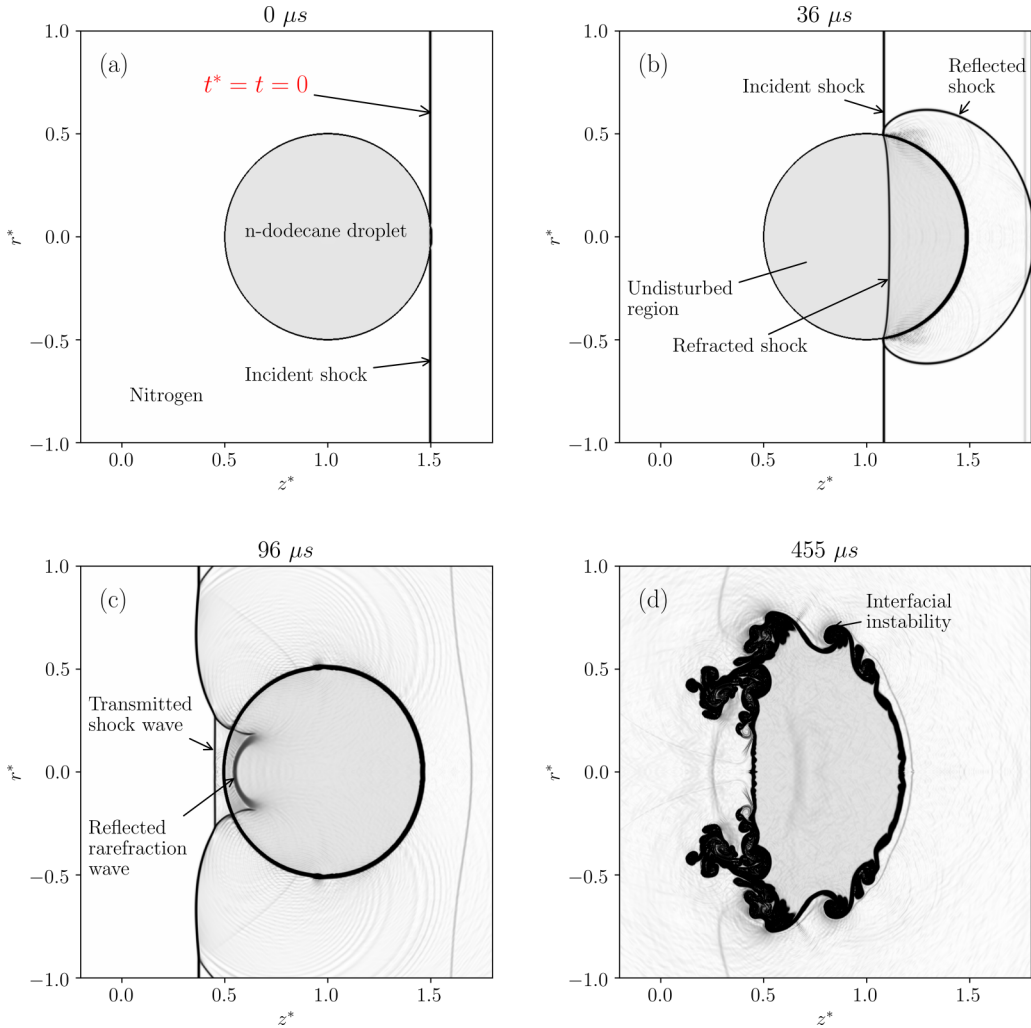


FIG. 6. Computational Schlieren images for the Mach 1.2 shock interaction with a fuel (*n*-dodecane) droplet ($T_{\text{PRE}} = 545.7 \text{ K}$ and $p_{\text{PRE}} = 6 \text{ MPa}$) at (a) $0 \mu s$, (b) $36 \mu s$, (c) $96 \mu s$, and (d) $455 \mu s$.

1. The transition from diverging to converging behavior

An important result of varying the temperature, T_{PRE} , is the changes to the SoS. The variations in the SoS with respect to temperature for nitrogen and *n*-dodecane are depicted in Fig. 7(a). The SoS for the surrounding fluid (nitrogen) increases with increasing temperature whereas the SoS for the fuel droplet (*n*-dodecane) reduces to a minimum near the pseudoboiling point [Fig. 7(a)]. Note that the pseudoboiling point for *n*-dodecane at 6 MPa occurs at the peak in the specific isobaric heat capacity at 730 K, where the fuel transitions from a liquidlike to a gaslike supercritical fluid [Fig. 7(c)].

As discussed in Sec. II D in conjunction with Fig. 2, the classification of diverging [Fig. 2(a)] and converging [Fig. 2(b)] cases is achieved using the ratio between the SoS of the surrounding fluid and the fuel droplet, n [Eq. (8)]. In Fig. 7(d), we show the change in n with respect to temperature. When the ratio, n , is less than unity (i.e., 500 K), it becomes a diverging shock-droplet interaction [Fig. 7(d)] whereas when the ratio, n , is greater than unity (i.e., 650 or 800 K) it implies that the

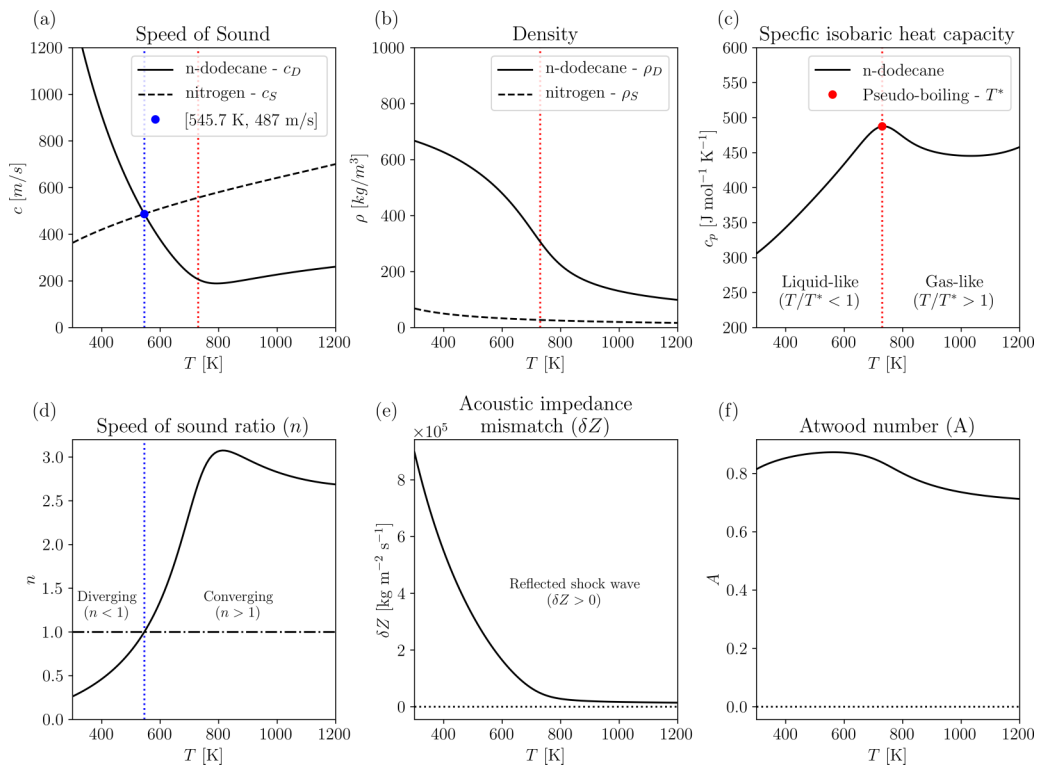


FIG. 7. (a) SoS and (b) density variation with respect to the temperature for nitrogen and *n*-dodecane at 6 MPa. (c) Change in specific isobaric heat capacity for the *n*-dodecane, where the red dotted line corresponds to the pseudoboiling point temperature (T^*) of *n*-dodecane where the specific isobaric heat capacity reaches a peak. The depiction includes the change in (d) the SoS ratio (n), (e) the acoustic impedance mismatch (δZ), and (f) the Atwood number (A). The blue dotted line is the temperature (545.7 K) where the SoS of the *n*-dodecane and the nitrogen are equivalent (≈ 487 m/s, $n = 1$).

shock-droplet interaction is converging. The transitional point from diverging to converging ($n = 1$) occurs at approximately 545.7 K at 6 MPa. Additionally, Fig. 4 shows a green dotted line on the phase diagram where $n = 1$.

Figure 8 elucidates the transition from a diverging ($n < 1$) to a converging ($n > 1$) refracted shock wave. The 500-K case is an example of a diverging case where the SoS is greater in the droplet than in the surrounding fluid, resulting in a diverging refracted shock [Fig. 8(a)]. The 650-K case is an example of a case where the SoS is less in the droplet than in the surrounding fluid, resulting in a converging refracted shock wave [Fig. 8(c)]. For the 545.7-K case, the refracted shock wave travels at approximately the same speed as the incident shock and, therefore, is neither diverging nor converging [Fig. 8(b)].

The TSDI differs significantly from classical SDI and SBI interactions. Throughout the following sections, we make comparisons with these classic SBI and SDI cases that are presented in Appendices B and C. In Fig. 8, the subcritical liquid water SDI (divergent) case [Fig. 8(d)], the classic divergent SBI case [helium bubble, Fig. 8(e)], and the classic convergent SBI case [R22 bubble, Fig. 8(f)] are compared. The convergent fuel-droplet case [Fig. 8(c)] and the classic convergent SBI case [Fig. 8(e)] exhibit the same shock-interaction behavior. The key differences are between the fuel-droplet divergent case [Fig. 8(a)] and the classic divergent SBI case [Fig. 8(d)]. As discussed previously, in the classic divergent SBI case, the reflected wave is a rarefaction wave; however, in the fuel-droplet divergent case [Fig. 8(a)], the reflected wave is a shock wave due to the impedance

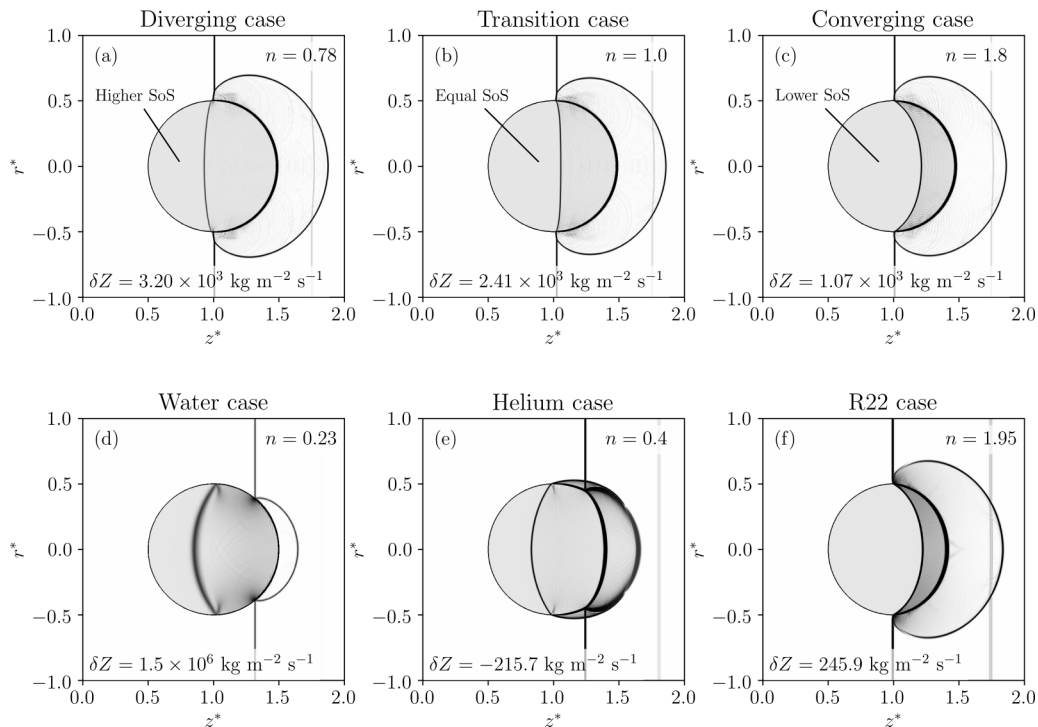


FIG. 8. Depiction of the three TSDI cases that differ in temperature: (a) 500 K ($n = 0.78$), (b) 545.7 K ($n = 1$), and (c) 650 K ($n = 1.8$). As a result, the refracted shock behavior changes from a diverging shock to a converging shock case. Additionally, (d) shows the divergent water SDI case, (e) shows the divergent SBI case (helium bubble), and (f) shows the convergent SBI case (R22 bubble).

mismatch (δZ) [Fig. 7(e)]. This also means that the diverging fuel-droplet case [Fig. 8(a)] does *not* exhibit the twin regular reflection-refraction (TRR) formation of the classic diverging case [Fig. 8(e)]—the TRR formation is described in detail in Appendix B and annotated in Fig. 26. The fuel-droplet divergent case [Fig. 8(a)] has more in common with the divergent water droplet SDI case [Fig. 8(d)]—both cases result in a reflected shock wave due to the positive acoustic impedance mismatch (δZ). The key difference is that the acoustic impedance is much higher in the water droplet case and, as a result, the refracted shock is far weaker.

The TSDI provides an interesting link between the subcritical liquid SDI and supercritical or ideal-gas SBI. The diverging TSDI, where the fuel is in a *liquidlike* state, results in a diverging case where the shockwave behavior is like the classic *subcritical liquid* SDI, whereas the converging TSDI, where the fuel is in a *gaslike* state, results in similar shock behavior to the classic converging *ideal-gas* SBI. We will compare the later-time behavior of TSDI, SBI, and SDI in Fig. 12.

Figure 9 compares the temporal evolution of the TSDI of a converging case ($n = 1.8$) and a diverging case ($n = 0.75$) depicted using computational Schlieren images. For the diverging cases, the refracted shock wave moves ahead of the incident shock as it approaches the downstream face of the droplet [Fig. 9(a)]. The refracted wave is then reflected [Fig. 9(b)] and converges to a point [Figs. 9(c) and 9(d)].

For all the TSDI cases, the initial interaction of the shock wave and the droplet results in a high-pressure region between the refracted shockwave and the reflected shockwave [Figs. 10(a), 10(c), and 10(e)] that exceeds the postshock pressure of the incident normal shock wave (i.e., greater than 9 MPa). The focusing of the reflected wave within the droplet results in a low-pressure region where the pressure is well below the critical pressure of *n*-dodecane [Fig. 10(b)]. In this case,

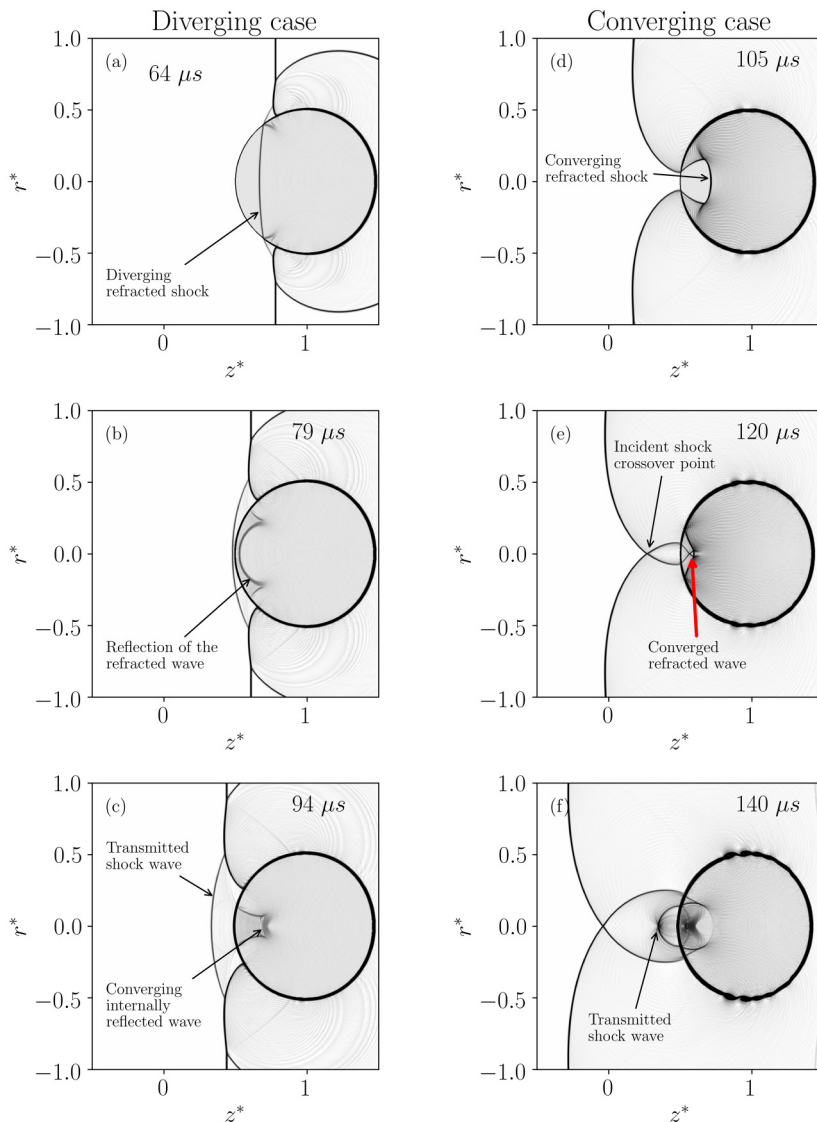


FIG. 9. Comparison of the (a)–(c) diverging case (500 K, $n = 0.78$) and the (d)–(f) converging case (650 K, $n = 1.8$).

the low-pressure region reaches a minimum of 0.5 MPa [Fig. 10(b)] which is below the critical pressure for the n -dodecane (1.82 MPa). This is a unique diverging case because it has a positive acoustic impedance mismatch [Fig. 8(a)] and, therefore, the internally reflected rarefaction wave. Typically, divergent cases have a negative impedance mismatch which is the case for the helium bubble validation problem [Fig. 8(d)] which, instead, results in an internally reflected shock wave as is shown in Fig. 26(d).

Conversely, as time progresses for the converging TSDI cases, the lower SoS in the n -dodecane (i.e., $n = 1.8$) becomes more apparent as the refracted shock lags further behind the incident shock as shown in Fig. 9(d). The shock wave dynamics of the convergent TSDI cases are consistent with the R22 convergent SBI case ($n > 1$) [see Figs. 28(a)–28(c) and 29(a)–29(c) or Ref. [39]]. The

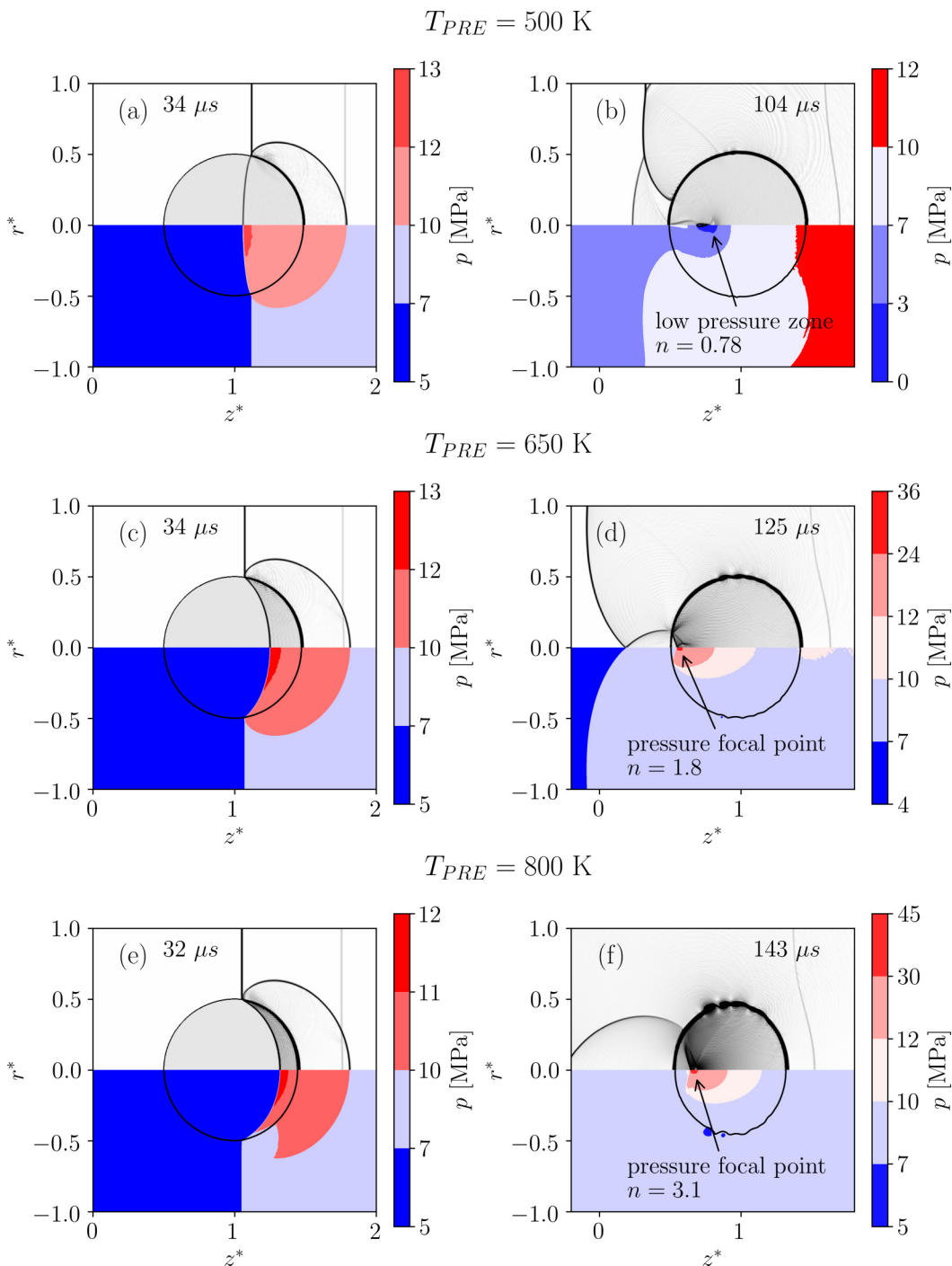


FIG. 10. Depiction of the diverging case (a), (b) $T_{PRE} = 500$ K where the reflection of the refracted shock results in a localized low-pressure region compared to the converging cases—(c), (d) $T_{PRE} = 650$ K and (e), (f) $T_{PRE} = 800$ K—when the converging refracted shock wave reaches a focal point, resulting in high localized pressures. The top half of the frame is the computational Schlieren image, and the bottom half of the frame is the pressure distribution.

refracted wave converges to a focal point as is annotated in Fig. 9(e) resulting in the emission of a transmitted shock wave annotated in Fig. 9(f).

The computational Schlieren images and pressure distribution at the time of full convergence to the focal point are depicted in Figs. 10(d) and 10(f) for the two convergent cases (650- and 800-K cases). The focal point of the refracted shock convergence results in high localized pressure on the downstream side of the droplet [Figs. 10(d) and 10(f)]. For the 650-K case ($n = 1.8$), the maximum pressure is 36 MPa, whereas for the 800-K case ($n = 3.1$) the maximum pressure is about 45 MPa. Note that, as n increases, the focal point of the converging shock moves inward [further away from the downstream interface, Figs. 10(d) and 10(f)]. A peak in n is found to occur at about 800 K [see Fig. 7(d)]. The localized maximum pressure caused by the convergence of the refracted shock wave results in the formation of an axial jet that will be illustrated in detail in Fig. 11. If the convergence occurs within the droplet, this jet is directed outwards [Figs. 10(d) and 10(f)]. This phenomenon has been observed for the convergent R22 SBI case [38,39] [Figs. 28(e)–28(h) and 29(e)–29(h)].

To further investigate the jet formation in converging cases, in Fig. 11, we focus on the temporal variation of the axial pressure for the 650-K case where the refracted shock convergence occurs just inside the droplet near the downstream interface. Figure 11(a) shows the point in time where the refracted shock has fully wrapped around the undisturbed droplet region and is near the focal point. Figure 11(b) shows the axial pressure distribution before the shock wave convergence, where the leftward traveling shock exhibits a significant pressure peak of about 18 MPa. There is no more undisturbed region once the shock converges [Fig. 11(c)] and the peak pressure at the axis near the downstream interface reaches about 30 MPa [Fig. 11(d)]. After the shock convergence, the shock wave is reflected as a strong rarefaction wave as seen in Figs. 11(e) and 11(f) where the pressure drops to below 5 MPa.

In Fig. 12, we compare the fuel droplet shape with the SDI and SBI cases at later times ($t^* = 0.6$). It is immediately apparent from Fig. 12 that the TSDI droplet shape expands radially like the SDI case [Fig. 12(b)] and develops interfacial instability comparable to the R22 SBI [Fig. 12(b)]. The helium SBI results in a very different shape—a kidney-shaped formation [Fig. 12(d)]—due to the very low density of the helium bubble compared to the surrounding air (see Appendix B for more details). The primary differences between these cases are related to the density ratio (ρ_D/ρ_S). At supercritical pressures, the density ratio between the fuel droplet and the surrounding nitrogen (ρ_D/ρ_S) varies from ≈ 9 to ≈ 31 for the cases considered in the present paper, whereas the density ratio ranges from ≈ 0.14 (helium) to ≈ 3.1 (R22) for the SBI cases and ≈ 831 for the SDI case (water). Hence, the TSDI droplet shape [Fig. 12(a), $\rho_D/\rho_S = 14$] exhibits similarities with the SDI [Fig. 12(b), $\rho_D/\rho_S = 833$] and the R22 SBI [Fig. 12(c), $\rho_D/\rho_S = 3.1$], and has less in common with the helium SBI [Fig. 12(d), $\rho_D/\rho_S = 0.14$].

2. Vorticity generation and flow circulation

Quantifying the vorticity deposition is of interest when analyzing the physical mechanisms that occur during SDI or SBI interactions (Appendices B and C). Like the classical SDI and SBI cases, the hydrodynamic instabilities at the interface in TSDI are initiated by impulsively accelerating two fluids of different densities—Richtmyer-Meshkov instability (RMI) [110,111]. This creates a baroclinic vorticity deposition on the interface. To better understand the growth of instabilities at later times, and eventually the breakup process, we start with portraying the evolution of the baroclinic vorticity in TSDI.

As discussed earlier (Sec. II B), the primary source of vorticity is the baroclinic vorticity due to the misalignments of local pressure and density gradients of the interface, that is, $\frac{1}{\rho^2} \nabla \rho \times \nabla p$ [see Eq. (7)], and the passage of the shock across the droplet results in significant generation of baroclinic vorticity. For the three T_{PRE} cases, the shock wave pressure gradients (∇p) are almost equivalent for the Mach 1.2 shock wave in nitrogen as outlined in Table I. This is because the pressure jump across a normal shock depends on (1) the shock strength (i.e., Mach 1.2) and the (2) specific heat ratio (γ) of the fluid (γ of nitrogen only varies between 1.446 and 1.391 from 500 to

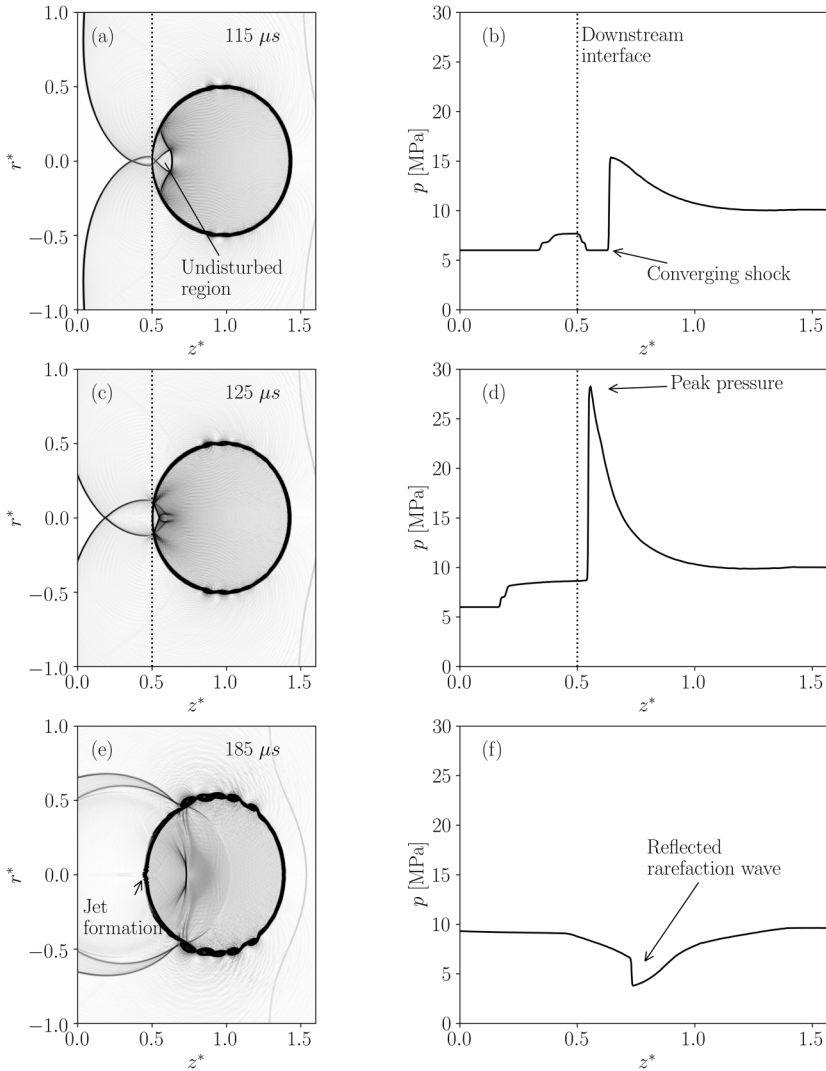


FIG. 11. The computational Schlieren images (a), (c), (e) and the corresponding axial pressure distributions (b), (d), (f) for $T_{\text{PRE}} = 650 \text{ K}$, $p_{\text{PRE}} = 6 \text{ MPa}$, and Mach 1.2. The depiction shows the shock convergence resulting in a localized high-pressure region inside the downstream droplet interface. The pressure peak in (d) causes the formation of an axial jet.

800 K). The density gradient, however, varies significantly as the droplet, which is at supercritical pressure, transitions from a liquidlike to a gaslike supercritical fluid [Fig. 3(b)]. The density and vorticity distributions for the three cases (500, 650, and 800 K) are depicted in Fig. 13 for the same nondimensional time $t^* = 0.38$. The higher density of the droplet compared to the nitrogen environment results in the generation of positive vorticity as the shock wave propagates through the droplet as shown in Fig. 13. Another unique feature of the TSDI is that the rotational direction of the generated baroclinic vorticity is the same for both the divergent and convergent cases (Fig. 13). In the divergent (helium) and convergent (R22) SBI cases, the vorticity rotation direction of the helium bubble case is in the opposite direction to the vorticity of the R22 case (Fig. 30): this is due to the low density of the helium bubble case ($A < 0$) and the high density of the R22 case ($A > 0$) [48]. For

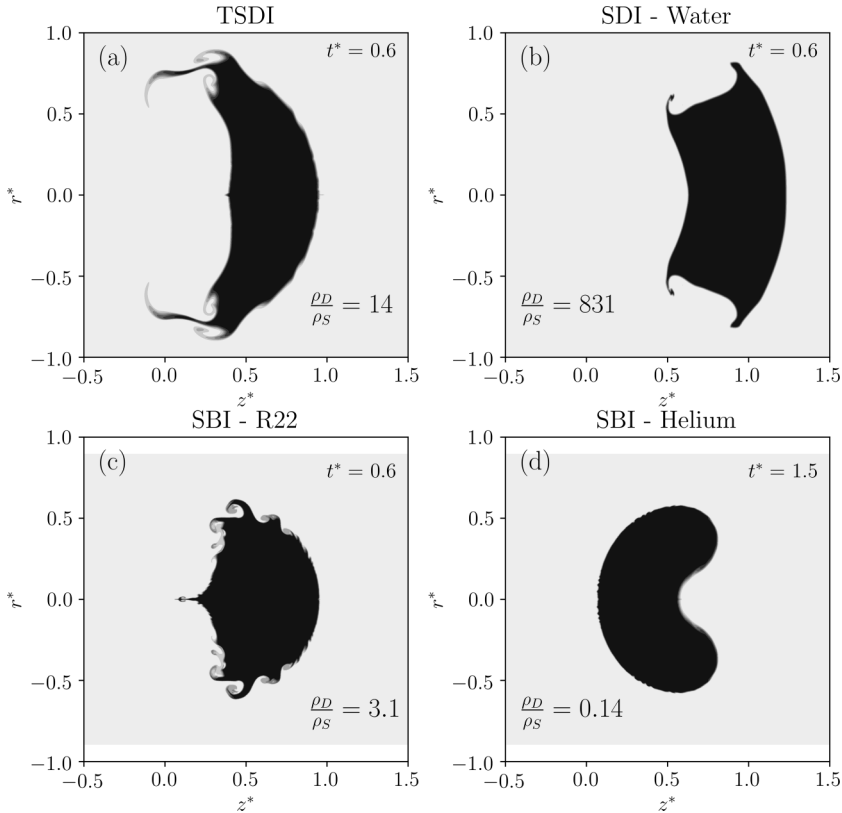


FIG. 12. (a) The droplet shape for the TSDI after the shock interaction compared to (b) the SDI where the droplet is water and the SBI cases: (c) R22 and (d) helium. Note that the nondimensional breakup time is less relevant for the helium SBI case, hence the greater value of $t^* = 1.5$ in (d).

the n -dodecane droplet, the Atwood number is always positive [Fig. 7(f)] and, therefore, the bulk of the vorticity generation is positive for a shock wave traveling from right to left past the droplet.

The total flow circulation for the same cases (i.e., $T_{\text{PRE}} = 500, 650,$ and 800 K) is shown in Fig. 14(a). In Fig. 14, the beginning of the shock crossover is indicated by the plus symbols (+) and the first appearance of the transmitted shock is indicated by a closed circle symbol (\bullet). Figure 14 includes the computational Schlieren images when the crossover shock first appears [Fig. 14(b), 800 K; Fig. 14(e), 500 K] and when the transmitted shock first appears [Fig. 14(c), 800 K; Fig. 14(d), 500 K]. In the divergent case (500 K), the transmitted shock appears before the crossover begins because the refracted shock reaches the downstream interface long before the incident shock is diffracted around the droplet. In the convergent cases (650 and 800 K), where the transmitted shock appears after the crossover point, there is a drop in flow circulation after the appearance of the transmitted shock due to the transmitted shock interacting strongly with the droplet interface. This behavior is consistent with the R22 convergent SBI case (Fig. 31).

Figure 14(a) demonstrates that the flow circulation increases rapidly as the incident shock passes over the droplet and interacts with the n -dodecane and nitrogen interface until the shock crossover. It is also interesting to note that this initial rate of circulation increases with increasing temperature [Fig. 14(a)]. After the primary shock interactions are complete, the circulation more gradually increases (Fig. 14) due to the development of the interfacial instabilities as the droplet is accelerated by the postshock flow.

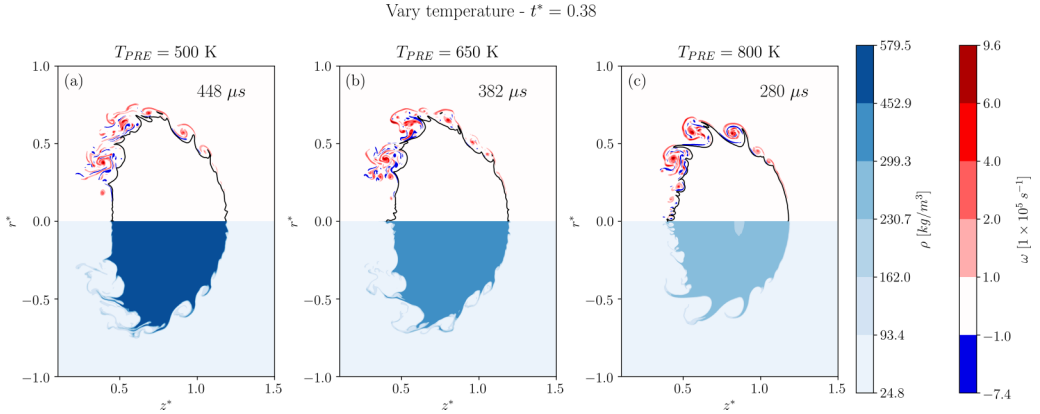


FIG. 13. The vorticity (top half) and density (bottom half) distributions for the three TSDI temperature cases (T_{PRE} : (a) 500 K, (b) 650 K, and (c) 800 K) when $t^* = 0.38$.

3. Droplet breakup and instability

In Ref. [71], we made a conservative approximation of the surface tension $\sigma \sim 1 \times 10^{-3} \text{N/m}$ for the fuel TSDI case near the critical temperature. In Ref. [112], the Weber number for an SDI is defined as

$$\text{We} = \frac{\rho_{\text{POST}} u_{\text{POST}}^2 D_0}{\sigma}. \quad (13)$$

For the Mach 1.2 case where $T_{PRE} = 650 \text{ K}$ and $p_{PRE} = 6 \text{ MPa}$, the postshock state is provided in Table I. In this case, the approximate Weber number is $\text{We} \sim 5 \times 10^7$. This very large Weber number is due to the almost negligible surface tension near the critical point. As a result, the Weber number is $\text{We} > 10^3$, which means the TSDI cases are in the shear-induced entrainment breakup regime [112]. The resultant interfacial instability is shown in Fig. 13. By increasing the temperature at supercritical pressure, the fuel state changes significantly from a liquidlike to a gaslike supercritical fluid. As a result, the density changes significantly as shown in Fig. 13. All three cases show significant interfacial instability at the material interface and vorticity at the outer interface (away from the axis of symmetry).

An interesting feature of the higher temperature case (800 K) is the increase in the interface instability, especially at the downstream interface near the axis [Fig. 13(c)]. Because n is large, the shock convergent focal point occurs further from the downstream interface inside the droplet as is shown in Fig. 10(f). The stronger shock convergence ($n = 3.1$) results in a transmitted shockwave that interacts with a larger portion of the downstream interface. The more significant interaction of the transmitted shock wave with the downstream interface promotes interfacial instability.

B. Influence of the preshock pressure

Here, we consider how the preshock pressure (p_{PRE}) may change the TSDI. In Fig. 3, the influence of the pressure on the key properties of the n -dodecane and nitrogen system was presented. The important finding is that by changing the pressure we change the SoS ratio [see Fig. 3(c)]. The three cases we consider vary p_{PRE} from 2 to 6 and 10 MPa, keeping $T_{PRE} = 650 \text{ K}$ and the shock wave strength of Mach 1.2 constant. We chose $T_{PRE} = 650 \text{ K}$ for this paper because it is close to the critical temperature of n -dodecane (Fig. 4). It is important to note that the fuel in these pressure cases is below the pseudoboiling point, so it is in a supercritical liquidlike state (Fig. 3). The SoS ratio for all the cases discussed in this subsection remains above 1 ($n > 1$) and, thus, they all represent a convergent case.

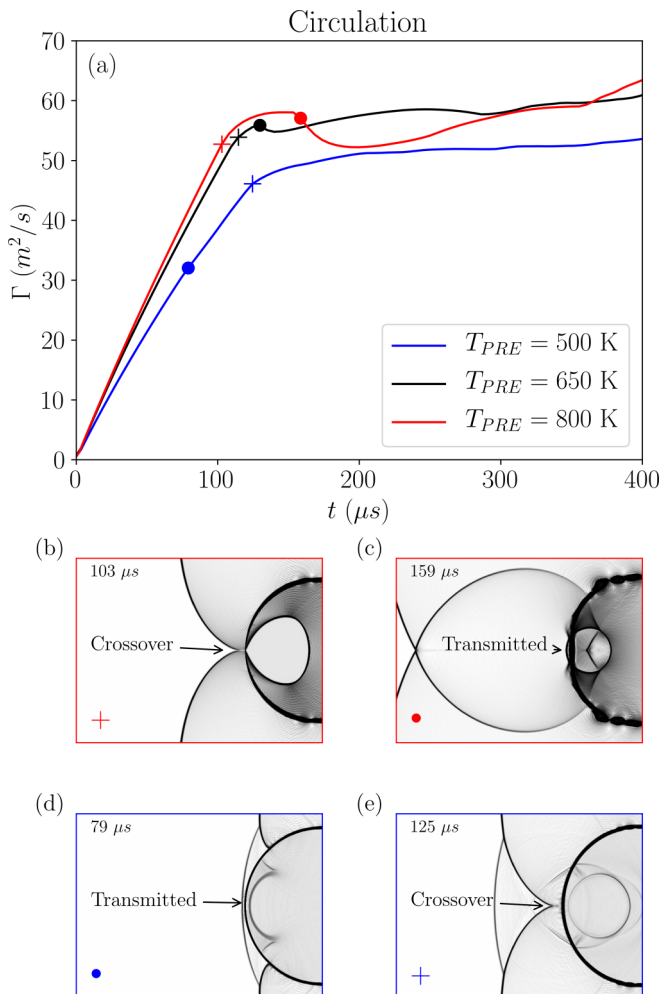


FIG. 14. Circulation of the flow with respect to (a) time (t) for the three temperature (T_{PRE}) cases (500, 650, and 800 K). The plus symbol (+) indicates the start of the shockwave crossover and the closed circle symbol (●) corresponds to the point in time when the transmitted shock first appears. The depiction includes the computational Schlieren images of the appearance of the crossover and transmitted shock for the 800-K case (b), (c) and the 500-K case (d), (e).

1. Weak and strong converging cases

Figure 15 illustrates the computational Schlieren images of the shock structures for two cases with a preshock pressure of 6 MPa ($n = 1.8$) and 10 MPa ($n = 1.43$). In both cases, the refracted shock travels slower within the droplet and the general shock wave pattern is found to be consistent with the convergent cases identified earlier for $n > 1$. However, the key difference between the 6-MPa ($n = 1.8$) and 10-MPa ($n = 1.43$) cases occurs at the later stages when the refracted shock nears the downstream interface [Figs. 15(b)–15(d)]. In the 6-MPa ($n = 1.8$) case, the outer shock crossover occurs before the refracted shock reaches the downstream interface, resulting in the refracted wave convergence to a focal point within the droplet [Fig. 15(d)]. Figure 15(b) shows that for a lower SoS ratio ($n = 1.43$) the focal point of the refracted shock does *not* occur within the droplet because the refracted shock wave reaches the downstream interface of the droplet before the incident shock has traveled around the droplet Fig. 15(b).

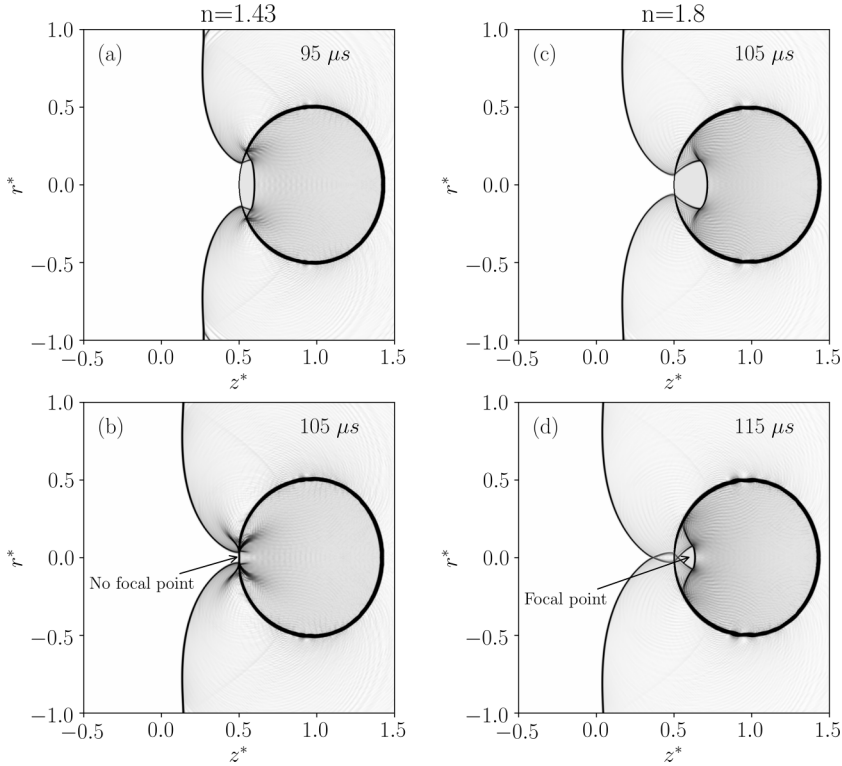


FIG. 15. Computational Schlieren images showing the evolution of the shock convergence for (a), (b) weak convergence ($p_{PRE} = 10$ MPa, $n = 1.43$) and (c), (d) strong convergence ($p_{PRE} = 6$ MPa, $n = 1.8$).

Figure 16 shows the pressure variation within the droplet along with the computational Schlieren images for $n = 1.43$. Figures 16(a) and 16(b) show that *no* focal point occurs within the droplet; instead, the refracted shock reaches the downstream pole. At a higher SoS ratio (i.e., $n = 1.8$), however, the incident shock wave travels faster around the outside of the droplet than the axial speed of the refracted shock speed—this results in a focal convergence point and the peak in pressure at the downstream interface of the droplet shown in Fig. 11(d). Consequently, instead of an *outward* axial jet that was a prominent feature of the convergent case with $n = 1.8$ (Fig. 11), an *inward* axial jet forms for $n = 1.43$ because of the low pressure of the reflected rarefaction wave [Figs. 16(c)–16(f)] and higher downstream pressure of the transmitted shock results in the slight inward deformation of the downstream interface at the axis of symmetry [Fig. 16(g)]. We are confident that this behavior is not a numerical artifact because this inward jet has been experimentally observed for a krypton SBI case that represents a case where the SoS ratio is about 1.5 ($n \sim 1.5$) (see Fig. 9 of Ref. [52]). Thus, we refer to the cases with a prominent outward axial jet as *strongly convergent* and *weakly convergent* if the axial jet is directed inward.

Here, we estimate the SoS ratio at which the shock interaction transitions from weakly convergent [Figs. 15(a) and 15(b)] to strongly convergent [Figs. 15(c) and 15(d)]. The transition case occurs when the incident shock wave outside the droplet reaches the downstream pole at the same time as the (internal) refracted shock as is schematically shown in Fig. 17. Assuming the Mach numbers of the shocks are equivalent (i.e., both Mach 1.2 in this case) and using the radius of the droplet (R) as an approximation to the shock curvature, the external shock wave will travel a distance of $3R$ and the refracted shock wave will travel $2R$ to reach the downstream pole (Fig. 17). Therefore, an SoS ratio of $n = 1.5$ that would result in the case where the external and internal shocks simultaneously reach

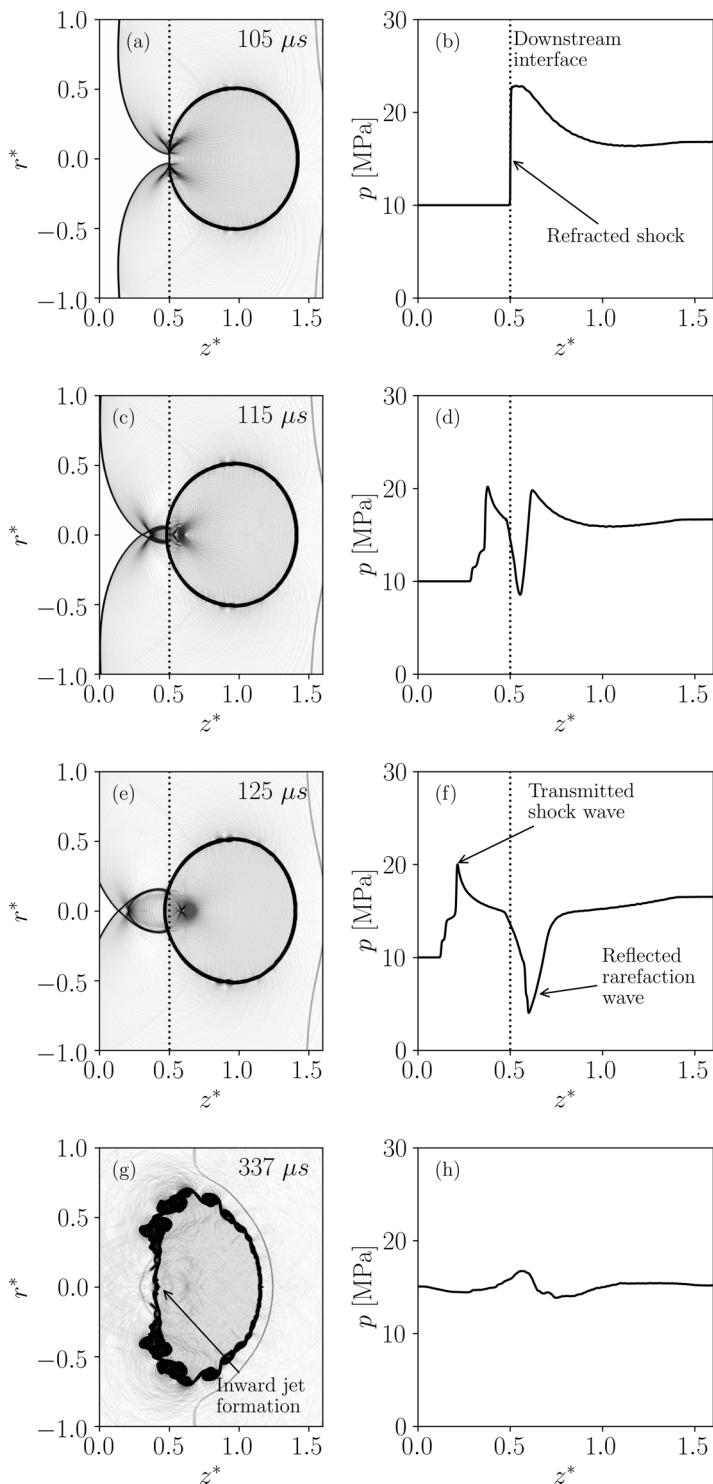


FIG. 16. The computational Schlieren images (a), (c), (e), (g) and the axial pressure distributions (b), (d), (f), (h) for the $p_{PRE} = 10$ MPa case which is considered as a weak convergent case where $n = 1.43$.

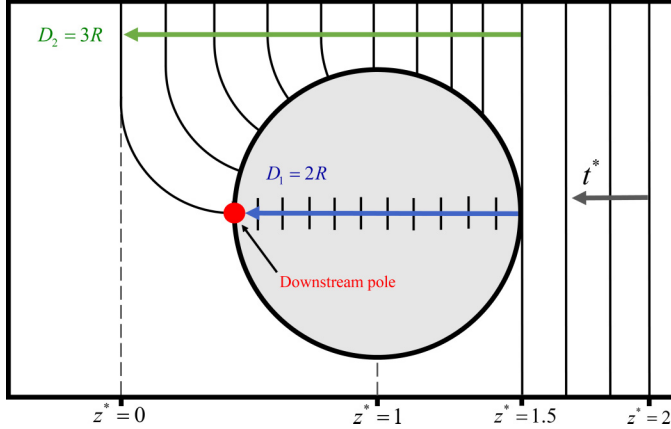


FIG. 17. Schematic of the approximate distance traveled by the incident shock ($D_2 = 3R$) and refracted shock ($D_1 = 2R$) to reach the downstream pole, where R is the droplet radius.

the downstream pole is the transitional SoS ratio from weakly convergent to strongly convergent. Thus, we hypothesize that the predicted transition SoS ratio from weakly convergent to strongly convergent occurs at $n = 1.5$. To test this hypothesis, we changed the ambient pressure to 9.8 MPa to mimic a condition at which the SoS ratio ($n = 1.48$) is close to the predicted value of $n = 1.5$. The shock pattern depicted in Figs. 18(a) and 18(b) shows that the incident shock and the refracted shock simultaneously reach the downstream pole. The incident shock far from the droplet approaches $z^* = 0$ when it reaches the downstream pole that corresponds to the $D_2 = 3R$ assumption made in Fig. 17. The discrepancy between the predicted transitional SoS ratio (i.e., $n = 1.5$) and the calculated value of $n = 1.48$ stems from the simplified assumptions made in this analysis. However, this simplified analysis proves our earlier assertion that transition from a weakly to a strongly convergent case, i.e., outward to inward axial jet, is related to the location at which the incident shock wave outside of the droplet and the refracted shockwave inside the droplet meet in relation to the downstream pole. Note that Fig. 4 includes a red dotted line on the phase diagram where $n = 1.48$.

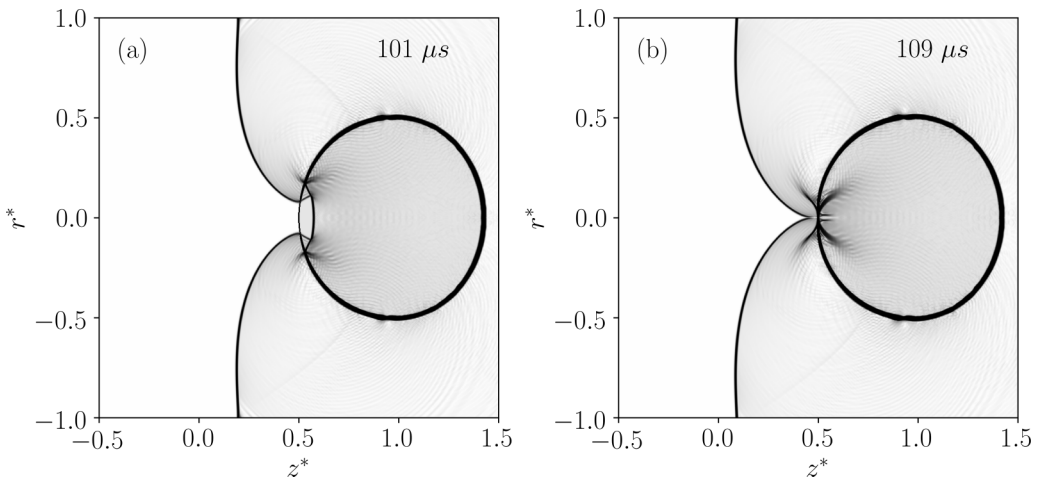


FIG. 18. Depiction of the convergence of the incident shock and the refracted shock on the downstream pole. This $p_{\text{PRE}} = 9.2$ MPa case ($n = 1.48$) is the transitional case from weakly convergent ($1 < n < 1.48$) to strongly convergent ($n > 1.48$).

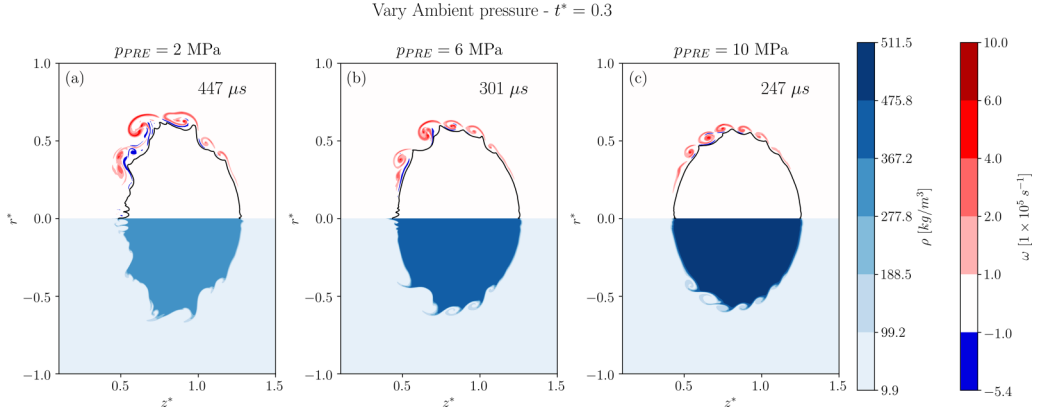


FIG. 19. The vorticity (top half) and density (bottom half) distributions for the three p_{PRE} cases (a) 2 MPa, (b) 6 MPa, and (c) 10 MPa at $t^* = 0.3$. Note that the numerical reconstruction is lowered to WENO3 to enable a direct comparison.

2. Vorticity generation and flow circulation

The vorticity and density distributions for three cases of varying preshock pressures (p_{PRE}) — 2, 6, and 10 MPa—are depicted in Fig. 19 where $T_{PRE} = 650$ K. One critical difference between these cases is that the n -dodecane and nitrogen density changes significantly approaching the critical pressure of n -dodecane (Table II). The temporal development of the total flow circulation depicted in Fig. 20 shows that the total flow circulation decreases with an increase in pressure. Again, this is likely due to the change in the baroclinic vorticity generation term $\frac{1}{\rho^2} \nabla \rho \times \nabla p$ [see Eq. (7)] which

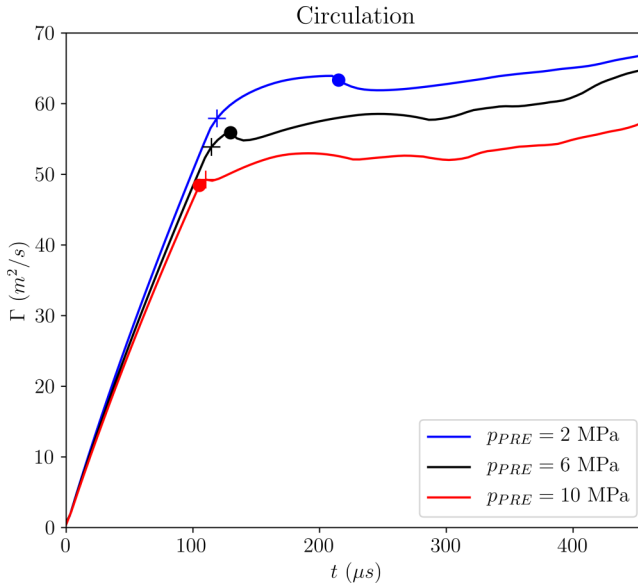


FIG. 20. Temporal evolution of the flow circulation for $p_{PRE} = 2, 6,$ and 10 MPa. The plus symbol (+) indicates the start of the shock wave crossover and the closed circle symbol (●) corresponds to the point in time when the transmitted shock first appears (see Fig. 14).

is highly dependent on the density. At higher pressures, the densities of both the n -dodecane and nitrogen increase, thus reducing the magnitude of the $1/\rho^2$ term.

Before the shockwave crossover occurs (indicated by the dots in Fig. 20), the flow circulation increases at a similar rate. Because the SoS ratio is much greater for the 2-MPa case ($n = 3.5$), the transmitted shock appears much later than in the 6-MPa case (Fig. 20). For the 10-MPa case, the transmitted shock appears before the crossover point (Fig. 20) due to the weak convergent behavior discussed previously in Sec. III B 1.

3. Droplet breakup and instability

Figure 19 shows the droplet shape and the unstable structures at $t^* = 0.3$ for different pressure conditions. It is noted that since the preshock temperature (T_{PRE}) is the same for all these cases the state of the fluid is considered liquidlike, and thus increasing the pressure does not drastically affect the droplet instability and the consequent droplet breakup. We showed in Sec. III A 3 that a more drastic change in the droplet behavior was observed by crossing the pseudoboiling temperature or the Widom line as the fluid transformed from a liquidlike to a gaslike state. Therefore, the preshock temperature imposes a more pronounced effect on the shock structure, and consequently the droplet deformation. Although the overall unstable structures are not significantly different for various pressures shown in Fig. 19, the physical time to reach this nondimensional breakup time is significantly longer, $447 \mu\text{s}$, for the 2-MPa case, compared to 301 and $247 \mu\text{s}$ for the 6- and 10-MPa cases, respectively. The growth of interfacial instabilities is faster for fuel droplets at higher pressures because the ratio of the postshock ambient density to the droplet density (i.e., $\sqrt{\rho_{\text{POST}}/\rho_D}$) increases with an increase in the preshock pressure, that is, $\sqrt{\rho_{\text{POST}}/\rho_D}$ equals 0.21 , 0.31 , and 0.37 for 2, 6, and 10 MPa, respectively.

The 2-MPa case is strongly convergent ($n = 3.5$) and results in amplified interfacial instabilities [Fig. 19(a)] compared to the higher-pressure cases, 6 and 10 MPa, where $n = 1.8$ and 1.43 , respectively [Figs. 19(b) and 19(c)]. This behavior is consistent with the strongly convergent behavior depicted in Fig. 13 and discussed in Sec. III A 3 for the cases that vary in temperature. The increase in interfacial instability is, again, due to the shock transmitted from the convergence focal point interacting more significantly with the downstream interface.

C. Influence of shock strength

We investigate the influence of varying the shock strength at a transcritical condition where $T_{\text{PRE}} = 650 \text{ K}$ and $p_{\text{PRE}} = 6 \text{ MPa}$. Similar to Sec. A, we chose the $T_{\text{PRE}} = 650 \text{ K}$ case because the temperature is the closest to the critical temperature of n -dodecane (Fig. 4), and it results in a converging case ($n = 1.8$) that has more complex transmitted shock behavior than the diverging cases ($n < 1.0$, i.e., $T_{\text{PRE}} = 500 \text{ K}$). The three shock strengths considered here are Mach 1.2, 1.6, and 2.0, where $n = 1.8$ for all cases (Fig. 4). The initial conditions, which are determined using the normal shock calculations and the PR-EoS, are provided in Table III. Note that n , δZ , and A are independent of the shock strength— $n = 1.8$, $R = 107\,400 \text{ kg m}^{-2} \text{ s}^{-1}$, and $A = 0.865$ for the conditions $T_{\text{PRE}} = 650 \text{ K}$ and $p_{\text{PRE}} = 6 \text{ MPa}$ (Table III).

Figure 21 compares the temporal evolution of the interface alongside the pressure contours for the three shock strengths (Mach 1.2, 1.6, and 2.0). This figure shows that by increasing the shock strength the transmitted shock wave and crossover shock wave shapes change significantly, influencing the shape of the droplet at later times [Figs. 21(c), 21(f), and 21(i)]. The transmitted shock wave and the crossover shock are annotated in Figs. 21(a) and 21(b). The position of the crossover point is marked by the vertical blue dotted line and the maximum radial distance traveled by the transmitted shock is depicted by the green dotted line. As the shock strength is increased, the transmitted shock travels less radially relative to the distance traveled axially (Fig. 21). For example, in Figs. 21(c), 21(f), and 21(i), the transmitted shock wave has traveled to $z^* = -1.1$ for all cases,

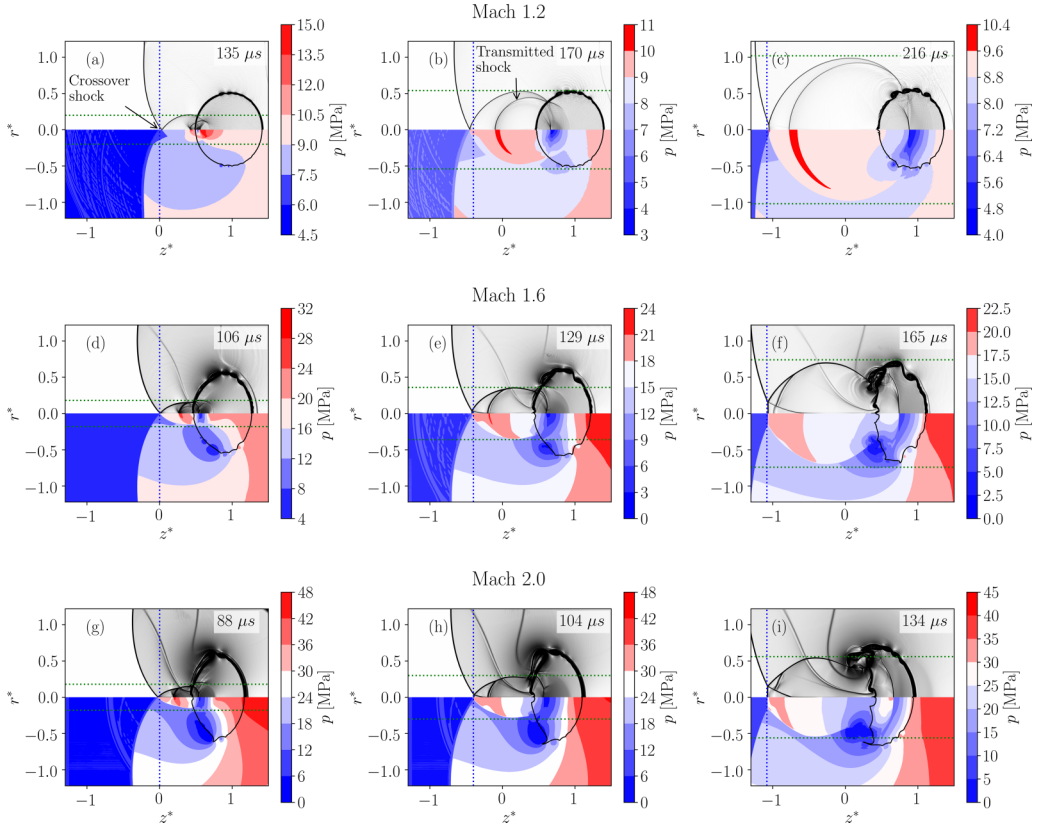


FIG. 21. The computational Schlieren images (top half) and pressure contours (bottom half) comparing downstream shock evolution for the various shock strengths (top row, Mach 1.2; middle row, Mach 1.6; and bottom row, Mach 2.0). The blue dotted line marks the shock crossover location and the maximum radial distance traveled by the transmitted shock is depicted by the green dotted line.

but radially the shock wave has reached a maximum distance of $r^* = 1.02$, 0.74 , and 0.56 for the Mach 1.2, 1.6, and 2 cases, respectively.

Another consideration is the average speed of the crossover shock in the radial direction relative to the axial speed. The crossover point moves downstream from $z^* = 0$ to -1.1 at Mach 1.21, 1.71, and 2.12 for the incident shock wave speeds of Mach 1.2, 1.6, and 2.0, respectively. So, the axial speed of the crossover point is close in magnitude to the incident shock speed. The radial expansion speed of the crossover shock for these cases decreases from Mach 0.9 to Mach 0.73 with an increase in incident shock speed from 1.2 to 2.0. This reduction in radial speed and increase in axial speed results in the narrowing of the crossover and transmitted shock formations observed by comparing the distance between the dotted green lines in Figs. 21(c), 21(f), and 21(i). Later in this section, we will show the effect of shock structures and speed on the geometry of the deformed droplet.

The downstream pressure distributions shown in the bottom half of Fig. 21 illustrate that the structure of the crossover shock wave and the transmitted shock wave changes with an increase in the shock strength. In the Mach 1.2 case, the high-pressure region associated with the evolution of the transmitted shock expands with almost the same rate in the radial and axial directions, as is implied by the distance between the dotted green lines in Figs. 21(a)–21(c). As a result, the droplet aspect ratio (radial to axial width) does change significantly in this case during the early development phase. Comparing Figs. 21(a) and 21(d) shows that by increasing the incident shock

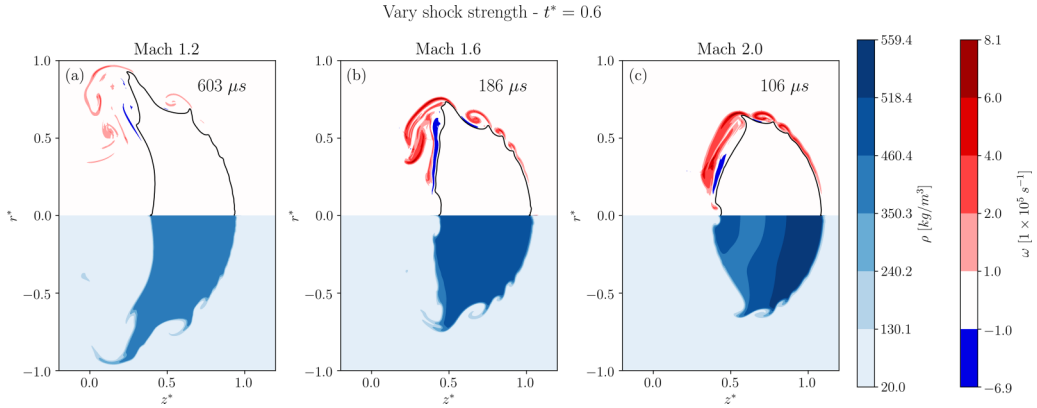


FIG. 22. The vorticity (top half) and density (bottom half) distributions for the three shock speed cases (a) Mach 1.2, (b) Mach 1.6, and (c) Mach 2.0 at $t^* = 0.6$. Note that $T_{\text{PRE}} = 650$ K, $p_{\text{PRE}} = 6$ MPa, and $n = 1.8$ for all cases. Note that the numerical reconstruction is lowered to WENO3 with the minmod flux limiter to enable a direct comparison.

strength to Mach 1.6 the pressure increase downstream of the transmitted shock is higher (about double in magnitude) and this high-pressure region is narrower in the radial direction compared with the Mach 1.2 case. The subsequent pressure distribution results in the axial squeezing of the droplet, forcing it to elongate radially to the low-pressure regions as shown in Fig. 21(e), increasing the droplet aspect ratio. This results in a pancake shape droplet at later times for the Mach 1.6 case [Fig. 21(f)], consistent with the experimental observation and computational results of SDI at subcritical conditions [25,32,36].

With a further increase in shock strength to Mach 2.0, the transmitted shock imposes a higher pressure distributed within a radially narrower region compared to lower incident shock speeds. This is evident by comparing the distance between the dotted green lines in Figs. 21(g)–21(i) with Figs. 21(d)–21(f). Like the Mach 1.6 case, the high downstream pressure behind the transmitted shock for the Mach 2.0 case results in the squeezing of the droplet; however, because this high-pressure region is radially less extended the droplet is not forced to elongate as far radially. Figure 22 compares the droplet shapes at the same nondimensional time of $t^* = 0.6$ to better represent the changes in the droplet aspect ratio for different tested incident shock strengths. This behavior is consistent with the results of increasing the shock strength when considering the shock interaction with a water column: the flattening or radial elongating of the water droplet is also found to reduce with shock strength due to the changes in the pressure distribution [68].

As previously stated, the three shock speed cases (Mach 1.2, 1.6, and 2.0) are all strongly convergent as $n = 1.8$ for all cases and exhibit slight outward jetting along the axis as indicated in Fig. 22. However, the downstream interface distortion varies significantly with increasing shock strength. It is observed in Fig. 22 that by increasing the shock speed the interface at the downstream pole is pushed inward (into the droplet) and this effect becomes more noticeable at later times. To better understand this phenomenon, Fig. 23 illustrates the pressure contours and the axial pressure distribution near the downstream interface after the transmitted shock appears for the three shock strength cases. Figure 23 shows that a high-pressure region is formed within the transmitted shock as it leaves the downstream interface, and a low-pressure region is generated within the droplet due to the reflected rarefaction wave. The subsequent pressure gradient at the downstream interface drives the interface inwards. Comparing the axial pressure distributions in Figs. 23(b), 23(d), and 23(f) reveals that the pressure gradient at the downstream pole of the droplet increases significantly with the shock strength, resulting in more noticeable interface indentation for the Mach 1.6 and the Mach 2 cases (Fig. 22). This inward deformation of the TSDI is not observed in the water SDI case—this

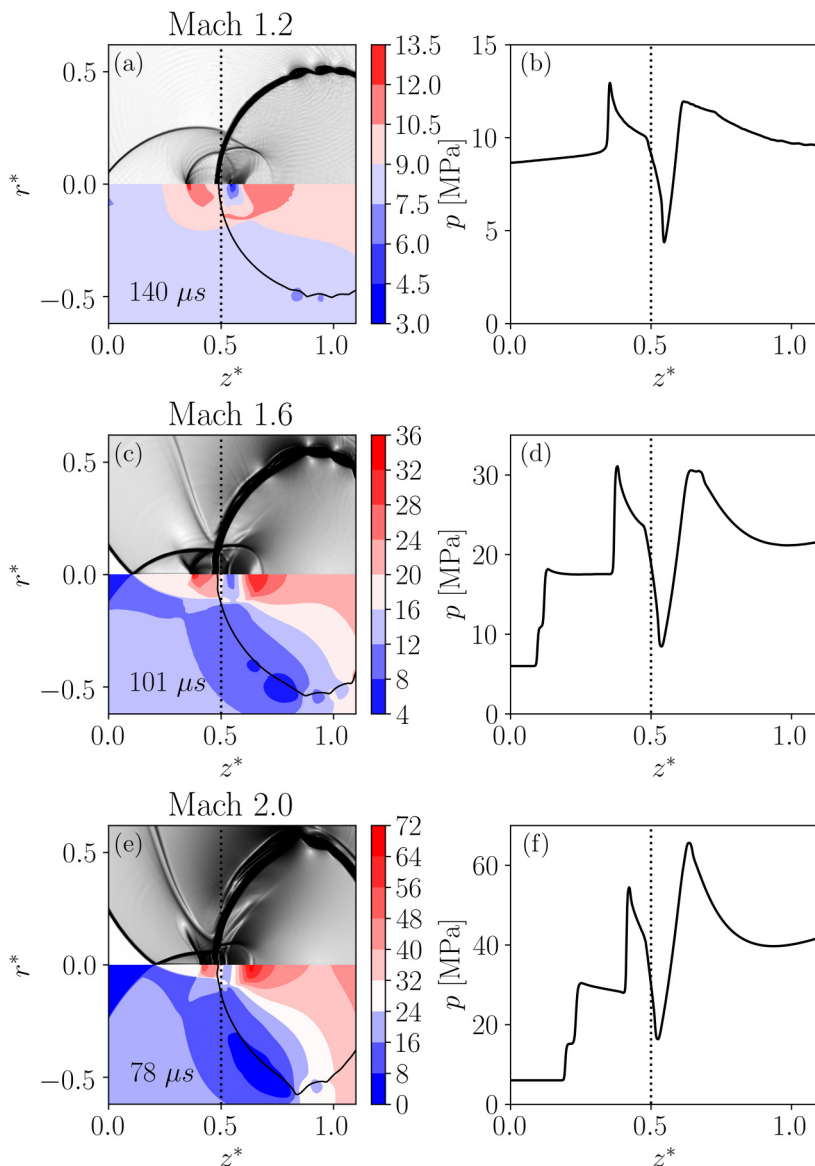


FIG. 23. Comparison of the pressure distributions after the transmitted shock appears downstream for the three shock strength cases: (a), (b) Mach 1.2, (c), (d) Mach 1.6, and (e), (f) Mach 2.0. The top half of (a), (c), and (e) shows the computational Schlieren images, and the bottom half shows the pressure contours. The corresponding axial pressure distributions for the three cases are depicted in (b), (d), and (f), respectively.

is because in the SDI case (1) the refracted shock is weak, (2) the refracted shock is divergent, and (3) the transmitted shock is insignificant (Fig. 32). Thus, the TSDI exhibits features that have *not* been observed in SDI cases.

Vorticity generation and flow circulation

The vorticity and density distributions for Mach 1.2, 1.6, and 2.0 at $t^* = 0.6$ are depicted in Fig. 22. As the density contours illustrate, the passage of the shock wave results in significant

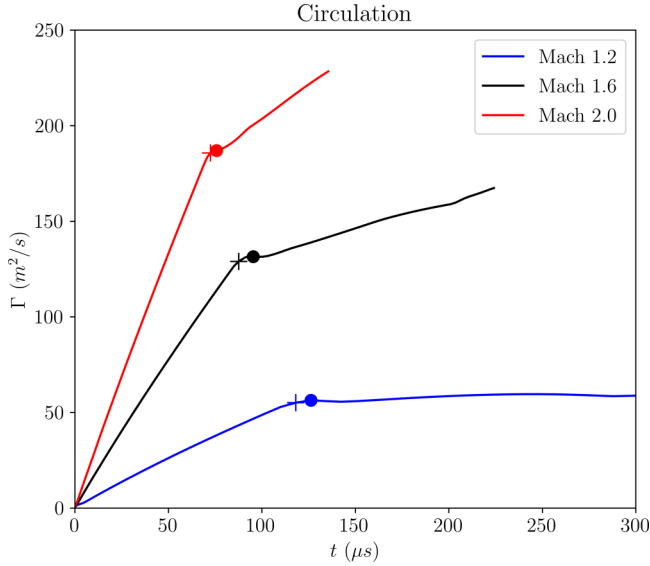


FIG. 24. Temporal evolution of the circulation for the three shock wave strengths (Mach 1.2, 1.6, and 2.0) at a preshock temperature of 650 K and preshock pressure of 6 MPa. The plus symbol (+) indicates the start of the shockwave crossover and the closed circle symbol (●) corresponds to the point in time when transmitted shock first appears (Fig. 14).

compression of the droplet that increases with the shock strength (Fig. 22). The vorticity contours illustrate that the deposition of the positive baroclinic vorticity at the interface creates a recirculation region behind the droplet that amplifies with an increase in shock strength. In the recirculation region behind the droplet, there is also negative vorticity generation which is consistent with the findings from the shock interaction with a water column presented in Ref. [68]. A large increase in the pressure jump across the normal shock is achieved with an increase in shock wave strength (Table III)— $\Delta p = 3.1, 11.0,$ and 21.1 MPa for Mach 1.2, 1.6, and 2, respectively. This increase in pressure jump results in the increased generation of baroclinic vorticity during the TSDI that is more evident by increasing the shock speed from Mach 1.2 to 1.6 [Figs. 22(a) and 22(b)]. This is also reflected in the evolution of the flow circulation for the three shock strength cases depicted in Fig. 24. This is consistent with the findings in Ref. [113] where researchers conducted an experimental study on the RMI mixing of an SF6 gas layer, where the vorticity and flow circulation increased with shock wave strength. The baroclinic vorticity deposition and flow circulation are expected to increase with Mach number for all shock-interface interaction cases—SBI, SDI, and TSDI.

To better disclose the early development of the circulation that is critical for understanding the TSDI at later stages, we presented the temporal variation of circulation. Figure 24 shows that the flow circulation increases more rapidly with increasing shock speed during the primary shock interaction (before the shock transmission and crossover) due to the increased pressure jump across the shock front and the fact that the shock travels faster past the droplet. As a result, the increase in shock strength directly leads to an increase in flow circulation (Fig. 24). Even after the shockwave interaction phase is complete, the flow circulation continues to increase at a higher rate for higher shock strengths. The increase in the postshock flow speed with increasing Mach number (Table III) increases the flow circulation and is expected to further amplify the interfacial instabilities.

In summary, increasing the shock strength at transcritical conditions does not significantly change the TSDI features as the SoS ratio (n) is independent of the shock strength. We showed that the increase in shock speed mainly affects the droplet morphology and its aspect ratio. Specifically,

the reduction in the fuel-droplet flattening with an increase in shock strength is consistent with the findings from the SDI case presented in Ref. [68]. The unique feature of the TSDI at higher shock strengths is the inward deformation of the fuel droplet at the downstream interface, which is not observed in the water SDI case.

IV. CONCLUSIONS

In this paper, we simulated the shock wave interaction with a fuel droplet at supercritical pressure (TSDI) and compared the shock and flow features with the classical SBI and classical SDI. The TSDI resulted in various interesting flow features including axial jetting and the formation of interfacial instabilities. Many of the flow features observed were consistent with the extensively studied SBI. However, we observed a transition from diverging to converging behavior due to the liquidlike to the gaslike transition of the fuel at transcritical conditions. This resulted in a unique case when the refracted shock diverges but the density of the fuel is higher than the surrounding fluid—this is more like a classic SDI case (i.e., shock interaction with a water droplet). SBI cases usually have a lower SoS for a dense gas (slower molecules), i.e., R22, whereas dense liquids typically have a higher SoS.

What makes the TSDI different from classic SDI is that the acoustic impedance mismatch is low enough for a significant refracted shock to be transmitted through the droplet—in the classic SDI case, the acoustic impedance is so high that only a very weak refracted shock is apparent. Subsequently, the TSDI behavior results in a transmitted shockwave and an internally reflected rarefaction wave that significantly changes the flow features, i.e., high-pressure, and low-pressure focal points within the droplet.

The TSDI differs from the classic SBI cases because the acoustic impedance mismatch is always positive while exhibiting both convergent and divergent behavior. SBI cases typically have negative acoustic impedance mismatch for diverging cases (i.e., helium) or positive acoustic impedance mismatch for converging cases (i.e., R22) due to the behavior of ideal gases. As a result, the diverging SBI results in (1) a reflected *rarefaction* wave, (2) a TRR formation, and (3) an internally reflected *shock wave*, whereas the diverging TSDI case involves (1) a reflected *shock wave*, (2) *no* TRR formation, and (3) an internally reflected *rarefaction* wave. Thus, the TSDI diverging case differs dramatically from a diverging SBI case.

The result showed the importance of the SoS ratio (n) on the interaction behavior with a transition from diverging to converging behavior at $n = 1$. Additionally, we observed a new transition point from a weakly convergent case to a strongly convergent case at $n \sim 1.48$. The strongly convergent behavior ($n > 1.48$) is where the refracted shock converges to a focal point within the bubble, often resulting in axial jetting. The weakly convergent behavior ($n < 1.48$) is where the refracted shock is too fast to converge to a point within the droplet, resulting in either insignificant axial jetting or inward jetting behavior.

Another consideration was the influence of shock strength on the TSDI behavior. As the shock strength was increased, the amount of droplet flattening reduced, which is consistent with the classic SDI behavior. A unique feature that appeared with increasing the shock strength is the inward deformation of the downstream interface. This inward deformation is found to be a result of the high pressure within the transmitted shock that has not been observed in classical SDI. Consequently, the TSDI cases have features in common with both SBI and SDI cases, providing an important link between these two widely studied problems.

The results presented in this paper provide important information about the early development of droplet breakup behavior and mixing efficiency for transcritical problems arising in high-pressure fuel injection. The model presented here will be used to simulate more specific transcritical problems, i.e., scramjets, ramjets, and liquid rocket engines. In future work, we plan on extending this model to three dimensions to further investigate the interfacial instability development and droplet breakup behavior at later times.

TABLE I. The changes to initial conditions for the four cases that change T_{PRE} : 500, 545.7, 650, and 800 K. The normal shock is Mach 1.2 and $P_{\text{PRE}} = 6$ MPa.

T_{PRE} (K)	500	545.7	650	800
ρ_{DROP} (kg/m ³)	567.2	531.5	419.9	223.5
ρ_{PRE} (kg/m ³)	39.65	36.3	30.46	24.79
ρ_{POST} [kg/m ³]	52.86	48.44	40.38	33.30
$u_{z,\text{POST}}$ [m/s]	-140.3	-146.7	-160.3	-178.0
p_{POST} [MPa]	9.1211	9.113	9.096	9.072
T_{POST} [K]	570.2	621.0	736.2	900.4
n	0.78	1.0	1.8	3.1
δZ [kg m ⁻² s ⁻¹]	320116	241314	107400	27913
A	0.869	0.872	0.865	0.80

ACKNOWLEDGMENT

Portions of this research were conducted with the advanced computing resources provided by Texas A&M High-Performance Research Computing.

APPENDIX A: CASE PARAMETERS

Here, we present all the parameters for the TSDI simulations. The normal shock wave relations [114] are used to approximate the postshock Mach number, pressure, and temperature:

$$M_{\text{POST}} = \sqrt{\frac{(\gamma^* - 1)M^2 + 2}{2\gamma M^2 - (\gamma^* - 1)}}, \quad (\text{A1})$$

$$p_{\text{POST}} = p_{\text{PRE}} \left(\frac{2\gamma^* M^2 - (\gamma^* - 1)}{\gamma^* + 1} \right), \quad (\text{A2})$$

$$T_{\text{POST}} = T_{\text{PRE}} \frac{[2\gamma^* M^2 - (\gamma^* - 1)][(\gamma^* - 1)M^2 + 2]}{(\gamma^* + 1)^2 M^2}, \quad (\text{A3})$$

 TABLE II. The changes to initial conditions for the four cases that change P_{PRE} : 2, 6, 9.2, and 10 MPa. The normal shock is Mach 1.2 and $T_{\text{PRE}} = 650$ K.

T_{PRE} [K]	2 MPa	6 MPa	9.2 MPa	10 MPa
ρ_D [kg/m ³]	310.7	419.9	455.1	461.9
ρ_{PRE} [kg/m ³]	10.3	30.46	46.18	50.05
ρ_{POST} [kg/m ³]	13.83	40.38	61.62	66.74
$u_{z,\text{POST}}$ [m/s]	-159.4	-160.3	-161.0	-161.2
p_{POST} [MPa]	3.034	9.096	14.0	15.2
T_{POST} [K]	731.4	736.2	740.0	741.0
n	3.5	1.8	1.48	1.43
δZ [kg m ⁻² s ⁻¹]	40450.4	107400	139572	146617
A	0.936	0.865	0.816	0.804
$\sqrt{\rho_{\text{POST}}/\rho_D}$	0.21	0.31	0.37	0.38

TABLE III. The changes to initial conditions (postshock properties) for the three cases that change in shock wave strength: Mach 1.2, Mach 1.6, and Mach 2.0. For these cases $T_{\text{PRE}} = 650$ K and $P_{\text{PRE}} = 6$ MPa ($n = 1.8$, $\partial Z = 107\,400$, $\text{kg m}^{-2} \text{s}^{-1}$, $A = 0.866$).

Shock strength	Mach 1.2	Mach 1.6	Mach 2.0
p_{POST} [MPa]	9.096	16.975	27.106
$u_{z,\text{POST}}$ [m/s]	-160.3	-426.2	-655.8
T_{POST} [K]	736.2	911.7	1114.1
ρ_{POST} [kg/m^3]	40.38	61.44	80.28

where the specific heat ratio (γ^*) is approximated using the PR-EoS [71,73]. We can then determine the postshock density of the nitrogen using the PR-EoS and the postshock velocity given by

$$u_{\text{POST}} = u_S \left(1 - \frac{M_{\text{POST}}}{M} \sqrt{\frac{T_{\text{POST}}}{T_{\text{PRE}}}} \right), \quad (\text{A4})$$

where u_S is the shock velocity.

APPENDIX B: SHOCK-BUBBLE INTERACTION

To validate the numerical model and understand the SBI at ideal-gas conditions (see Fig. 1), we consider two SBI problems that are commonly used in the literature. These problems involve the interaction of a Mach 1.2 shock with a bubble in an air environment: in this paper, we approximate the air using the properties of nitrogen. The two cases vary in the contents of the bubble: (1) helium (He) and (2) refrigerant R22 (CHClF_2). The key parameters for the validation cases that involve a leftward traveling Mach 1.2 shock wave that impacts a bubble (helium or R22) are outlined in Table IV.

1. Computational model

For the two shock-bubble validation cases, He- N_2 (Appendix B 2) and R22- N_2 (Appendix B 3), the 2D axisymmetric cylindrical computational domain is extended from -25 to 25 cm in the axial direction and 0 to 4.5 cm in the vertical direction as depicted in Fig. 25. Only the top half of the depicted computational domain is required for the simulation due to the axis of symmetry boundary condition at $r = 0$. The initial condition consists of a bubble (He or R22) at $z = 5$ cm and a leftward traveling normal shock (Mach 1.2) at $z = 10$ cm. The left and right boundaries use a transmissive boundary condition and the outer radial boundary at $r = 4.5$ is a reflective boundary, representing the rigid shock tube (Fig. 25). A uniform mesh is used between -16 and 16 cm where the cell dimensions are $\Delta z \approx \Delta r \approx 0.23$ mm. The mesh then grows in the z direction at approximately 10% to reach the ends of the domain.

TABLE IV. Key parameters for the validation cases involving a leftward traveling Mach 1.2 shock wave that impacts a bubble (helium or R22) with a diameter of 5 cm in a shock tube with a diameter of 9 cm.

Validation cases	Helium/nitrogen	R22/nitrogen
SoS ratio (n)	0.4 (divergent)	1.95 (convergent)
Acoustic impedance mismatch (δZ) ($\text{kg m}^{-2} \text{s}^{-1}$)	-215.7 (reflected rarefaction)	245.9 (reflected shock)
Atwood number (A)	-0.684	0.516

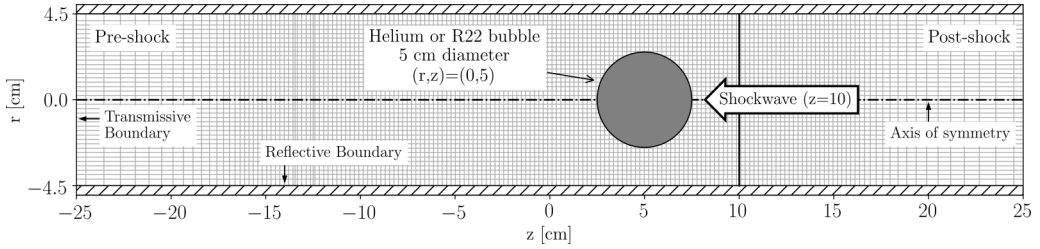


FIG. 25. Schematic of the shock-bubble interaction validation cases used for the helium bubble case and the R22 bubble case. The depicted cell size is ten times larger than the cell size used in the simulations ($\Delta z \approx \Delta r \approx 0.23$ mm). Due to the axis of the symmetry boundary condition, only the top half of the depicted computational domain is required for the simulation.

2. Helium shock-bubble interaction: A divergent case

The first case is the helium bubble which is used as a validation case in numerous numerical studies [39,89,97–106]. Here, we use the helium case to qualitatively and quantitatively validate our model. Figure 26 shows the numerical results which can be directly compared to the experimental results in Fig. 27 adopted from Ref. [38]. Note that throughout this paper $t = 0 \mu\text{s}$ is considered as the instant the incident shockwave first reaches the bubble interface—in this case, $t = 0 \mu\text{s}$ is when the incident shock reaches $z = 7.5$ cm and $t = -60 \mu\text{s}$ corresponds to the start of the simulations. The red contour line shows the material interface where the volume fraction of the helium is 0.95. After the leftward traveling Mach 1.2 shock (see Fig. 25) impacts the bubble, the refracted shock wave travels faster in the helium bubble due to the increased SoS ($n < 1$), resulting in a diverging refracted shock within the bubble, referred to as a divergent case as shown in Figs. 26(a), 26(b), 27(a), and 27(b). Due to the negative impedance mismatch, the reflected shock wave is a rarefaction wave as annotated in Fig. 26(a) and observed in Figs. 27(a)–27(e). The interaction of the incident shock wave with the bubble interface, in this case, results in a four-shock formation termed the TRR [39]—this is annotated in Fig. 26(c) and observed in Figs. 27(b) and 27(c). The TRR involves the formation of a side shock that connects the refracted shock to the incident and reflected shock wave with the development of an expansion wave (see Fig. 11 of Ref. [39] for a schematic of the phenomenon). The refracted shock later reaches the downstream bubble interface [Figs. 26(d) and 27(d)], resulting in the internally reflected shock and the transmitted shock [Fig. 26(e)]. Note that the definition of the transmitted shock in the literature is varied. In this paper, we refer to the shock formation that leaves the downstream interface as the *transmitted shock* [Fig. 26(e)] and the shock refracted within the bubble as the *refracted shock* [Fig. 26(a)]. The passage of the shock also induces baroclinic vorticity at the interface due to the density gradient of the interface and the pressure gradient of the shock wave [39] [see Eq. (7)]. In time, the vorticity from the shock passage induces a large jet that forms near the bubble axis of symmetry and deforms the bubble to a kidney shape [Figs. 26(g)–26(i) and 27(g)–27(i)].

To quantitatively validate the model, the speed of the incident shock (u_I), the speed of the refracted shock (u_R), and the speed of the transmitted shock (u_T) are calculated at the axis of symmetry and compared to the experimental results of Ref. [38] and the numerical results in Ref. [94]. Table V contains the quantitative validation results. The flow features of interest are annotated in Fig. 26. The shock speed measurements from the simulation for the incident shock speed (u_I) and transmitted shock speed (u_T) are all within the experimental range determined in Ref. [38], demonstrating acceptable quantitative agreement with less than 5% error. The refracted shock speed was found to be slightly higher (u_R), with an error of 9 and 13% compared to the benchmark results and the experimental results, respectively.

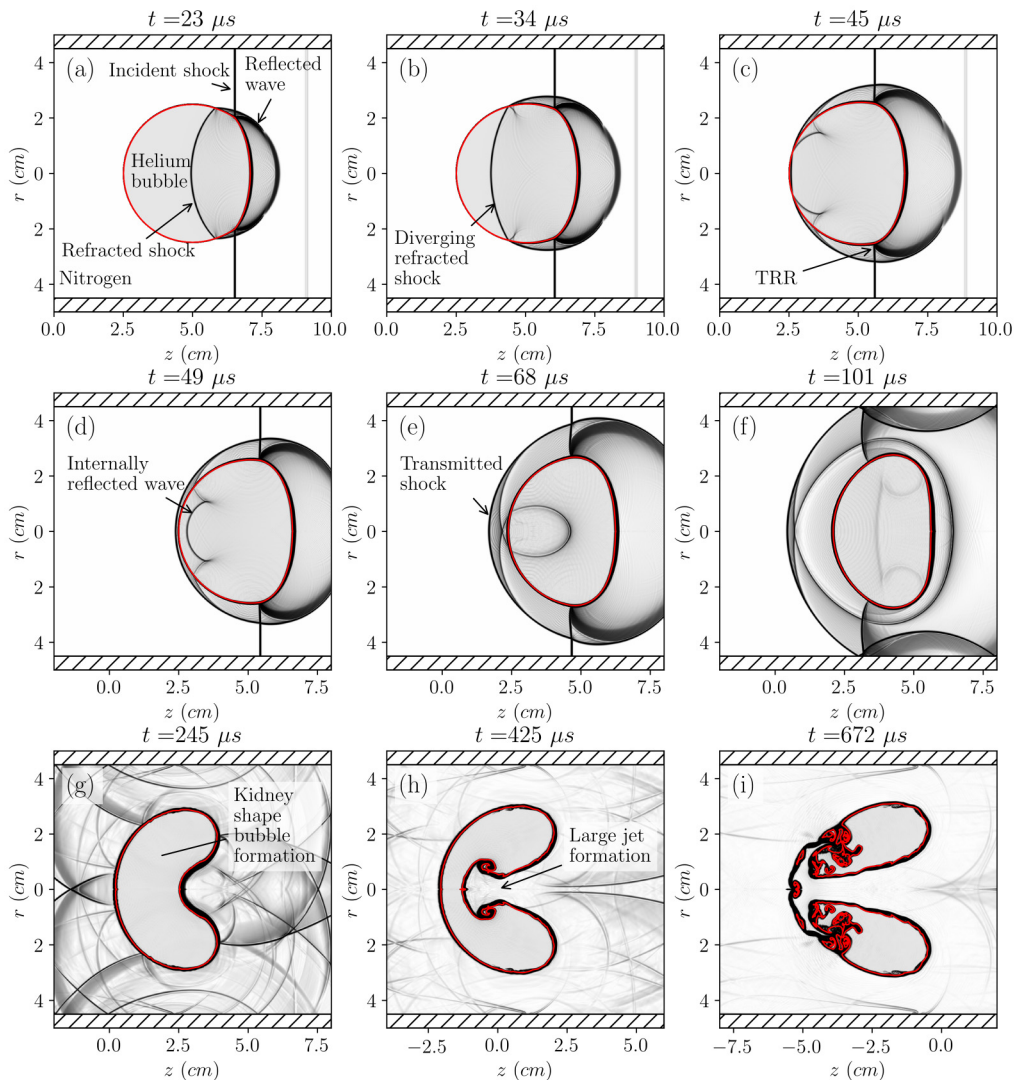


FIG. 26. Computational Schlieren images of the interaction of a Mach 1.2 shock with a helium bubble in a nitrogen environment at times (a) 23, (b) 34, (c) 45, (d) 49, (e) 68, (f) 101, (g) 244, (h) 425, and (i) 672 μs . The red contour line shows the material interface where $\alpha_D = 0.95$.

3. Shock-bubble interaction: A convergent case

The second validation case we consider in this section is the shock interaction of a Mach 1.2 shockwave with an R22 bubble in a nitrogen environment. This case is of interest because it exhibits a convergent refracted shock ($n > 1$) and the bubble is of a higher density than the surrounding fluid; thus, $\delta Z > 0$ and $A > 0$ (Table IV). In this case, the reflected wave in Figs. 28(a) and 29(a) is a shock wave because $\delta Z > 0$. The refracted shockwave that is shown in Figs. 28(a) and 29(a) is convergent due to the lower SoS of the bubble fluid ($n > 1$). The computational Schlieren images depict a key feature of the convergent case in Figs. 28(g), 28(h), 29(g), and 29(h) that is the formation of an axial jet as illustrated in Fig. 28(d) and experimentally captured in Fig. 29(d) [39,52–54]. The axial jet is created as the refracted shock converges to a focal point within the bubble near the

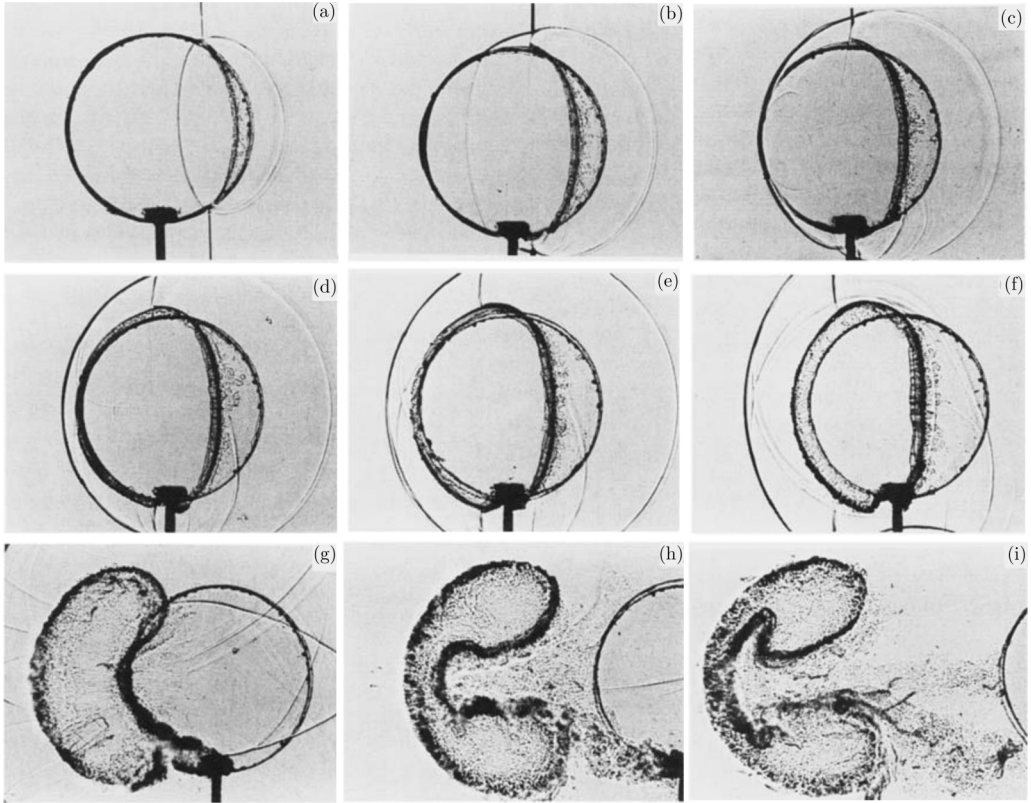


FIG. 27. Experimental Schlieren images of the interaction of a Mach 1.2 shock with a helium bubble in an air environment at times (a) 32, (b) 52, (c) 62, (d) 72, (e) 82, (f) 102, (g) 245, (h) 427, and (i) 674 μs . Experimental images reprinted with permission of the Cambridge University Press from Fig. 7 of Ref. [38].

downstream interface and creates a higher-pressure region. The red contour line shows the material interface at $\alpha_D = 0.95$, where α_D is the volume fraction of the bubble. Additionally, the refracted shock convergence to the focal point results in the formation of a transmitted shock annotated in Figs. 28(e) and 28(f) and observed in Figs. 29(e) and 29(f). The crossover shock, annotated in Fig. 28(d) and observed in Figs. 29(d) and 29(f), is due to the bubble changing the direction of the incident shock around the bubble resulting in the shock crossover. In general, a very good qualitative agreement is observed between the shock features and interface deformation between the simulations and experiments as well as acceptable quantitative results as outlined in Table V.

TABLE V. The quantitative validation of the shock speeds. The shock speed was determined by averaging the shock velocity along the axis of symmetry over the specified time interval. The table also includes the error (%) of our recorded shock speeds compared to the benchmark results and the experiment.

Shock speeds (m/s)	u_I	u_R	u_T
Time interval for averaging the shock speeds (μs)	-60 to 0	0 to 53	53 to 240
Simulation results from the present paper	426	1020	380
Benchmark [94]	420 (1.4%)	933 (9%)	362 (5%)
Experiment [38]	410 \pm 41 (3.9%)	900 \pm 90 (13%)	393 \pm 39 (3.3%)

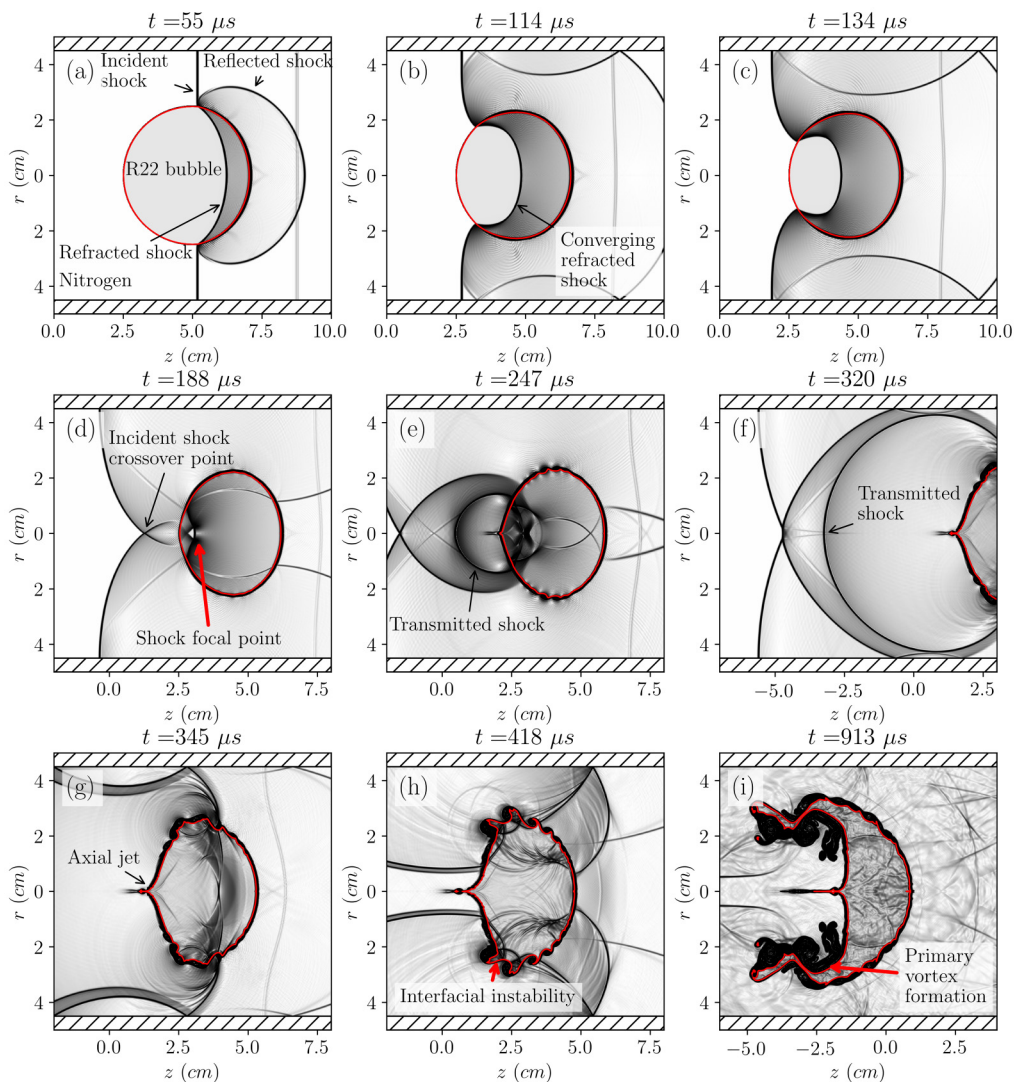


FIG. 28. Computational Schlieren images of the interaction of a Mach 1.2 shock with an R22 bubble in a nitrogen environment at times (a) 55, (b) 114, (c) 134, (d) 188, (e) 247, (f) 320, (g) 345, (h) 418, and (i) 913 μs . The red contour line shows the material interface where $\alpha_D = 0.95$.

Figure 30 shows the density and vorticity distributions for the helium and R22 cases during the shock interaction. The passage of the shock induces baroclinic vorticity at the interface due to the density gradient of the interface and the pressure gradient [Eq. (7)] [39] in both cases; however, the rotation in the helium case is in the opposite direction compared to the R22 case due to the change in density gradient direction at the material interface [48]. As a result, vorticity is predominantly negative in the helium case [Fig. 30(a)] and positive in the R22 case [Fig. 30(b)]. The generation of vorticity can be further interpreted by the total flow circulation shown in Fig. 31(a). In the R22 case where the refracted shock converges, the flow circulation increases to a maximum that occurs between the shock crossover indicated with a plus symbol (+) in Fig. 31(b) and shock transmission shown in Fig. 31(c). The closed circle symbol (\bullet) corresponds to the point in time when transmitted shock first appears.

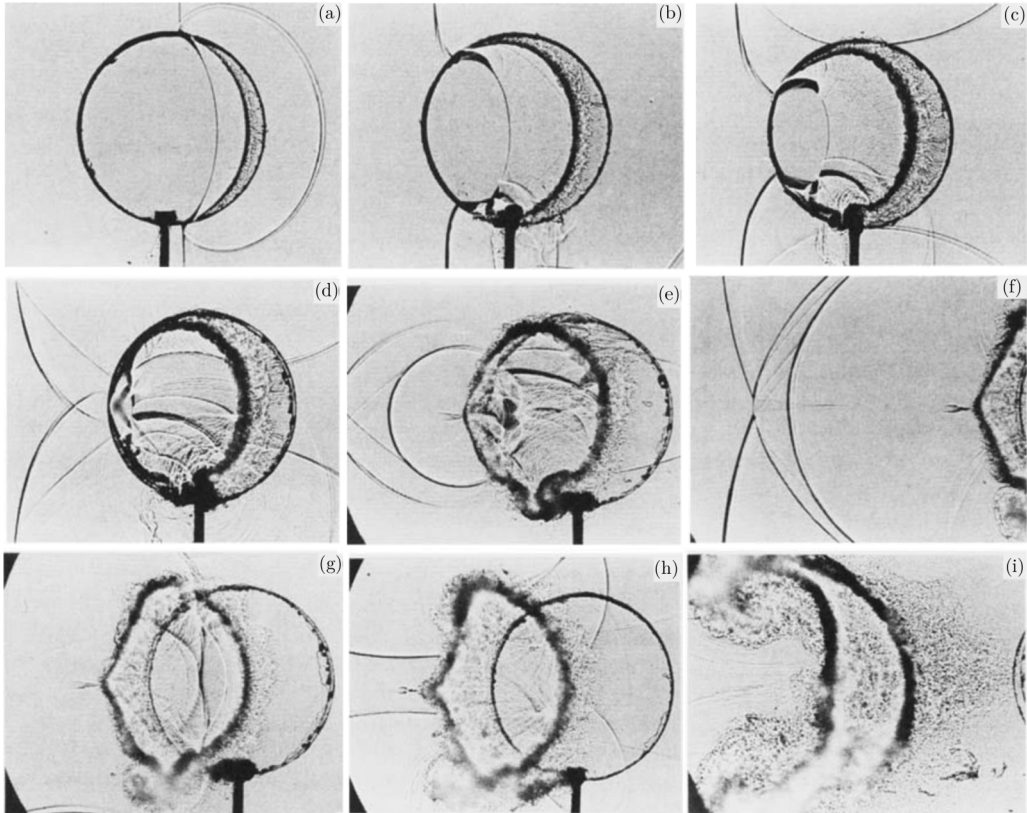


FIG. 29. Experimental Schlieren images of the interaction of a Mach 1.2 shock with an R22 bubble in an air environment at times (a) 55, (b) 115, (c) 135, (d) 187, (e) 247, (f) 318, (g) 342, (h) 417, and (i) 1020 μs . Experimental images reprinted with permission of the Cambridge University Press from Fig. 11 of Ref. [38].

In the helium case where the refracted shock diverges, the circulation sign is opposite to the R22 case consistent with the sign of the baroclinic vorticity stated above. The circulation reduces rapidly, reaching a local minimum when the shock transmission occurs as indicated with a closed circle symbol corresponding to Fig. 31(d).

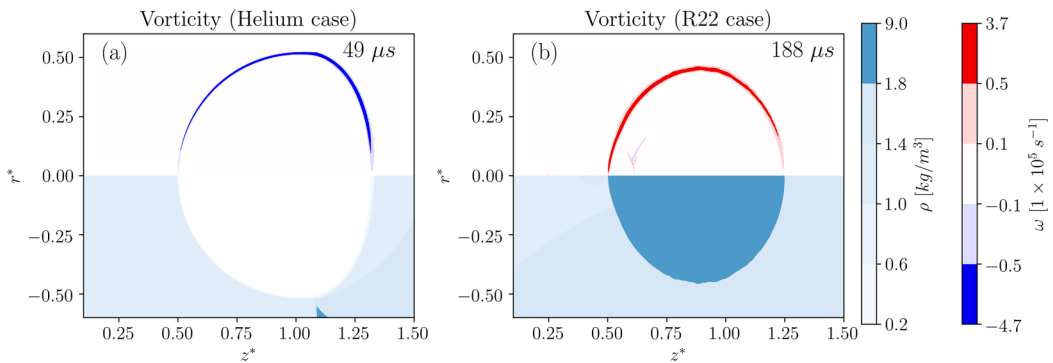


FIG. 30. The baroclinic vorticity (top half) and density distributions (bottom half) for (a) the helium bubble case and (b) the R22 bubble case. Panel (a) corresponds to Fig. 26(d) and panel (b) corresponds to Fig. 28(b).

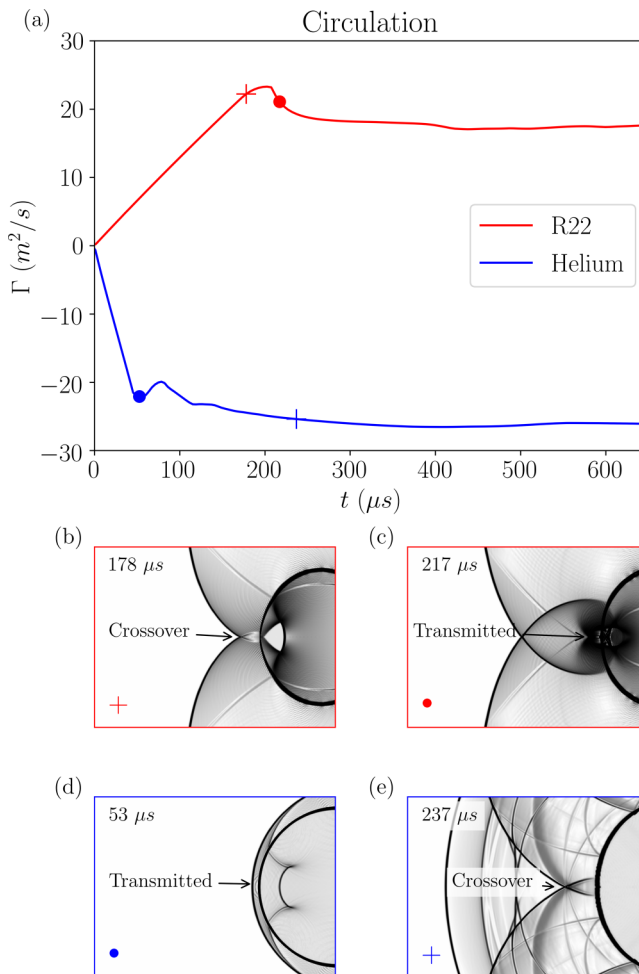


FIG. 31. (a) The temporal evolution of the total flow circulation for the helium and R22 cases. The plus symbol (+) indicates the start of the shockwave crossover and the closed circle symbol (●) corresponds to the point in time when transmitted shock first appears. The depiction includes the computational Schlieren images of the appearance of the crossover and transmitted shock for (b), (c) the R22 case and (d), (e) the helium case.

APPENDIX C: SHOCK-DROPLET INTERACTION

For comparison purposes, we consider here a shock interaction with a subcritical water droplet—this SDI case is considered in many studies [25,26,29,32,37,67,112,115,116]. To better model the liquid water droplet, we used the commonly used stiffened EoS and the fully conservative 5-Eq model [32,90,94,95,117]. The simulation was conducted using WENO3 reconstruction, RK3-TVD time stepping, and the HLLC approximate Riemann flux.

Figure 32 shows the Mach 1.2 shock interaction with the water droplet. Due to the large acoustic impedance mismatch ($\delta Z \sim 1.5 \times 10^6 [\text{kgm}^{-2}\text{s}^{-1}]$), a strong shock is reflected, and a weak shock is refracted within the droplet. Additionally, because of the stiffness of the water, the refracted shock results in a small density gradient requiring a large Schlieren shading function parameter ($k = 5 \times 10^5$ for the water and $k = 1 \times 10^4$ for the air) to visualize the refracted shock transmission

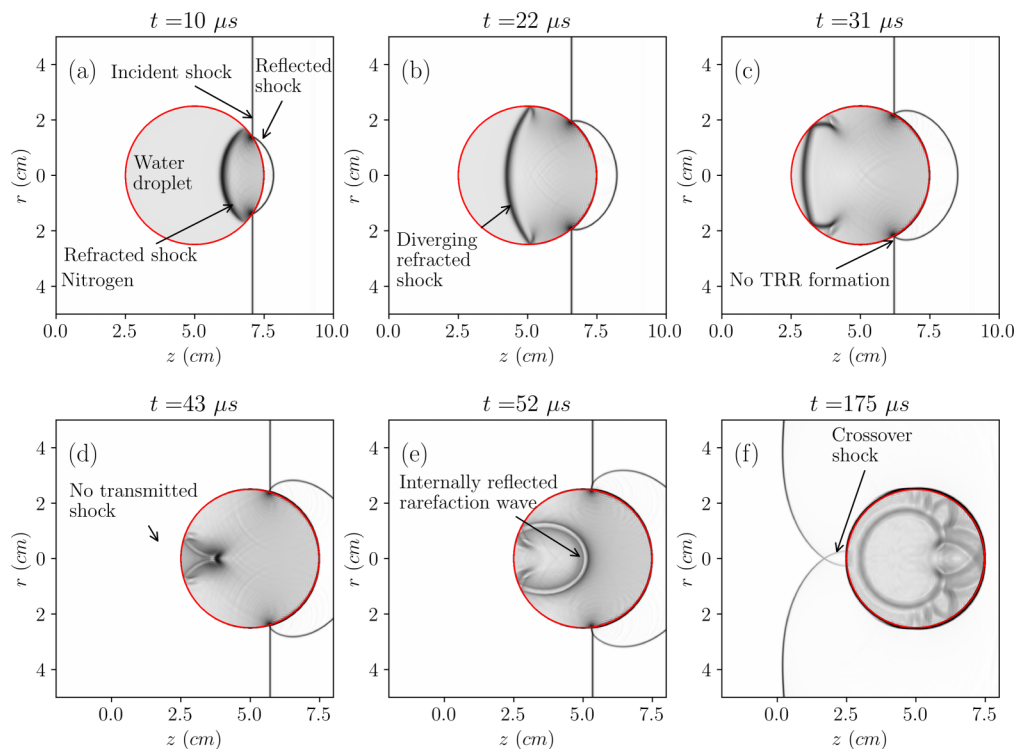


FIG. 32. Computational Schlieren images of the interaction of a Mach 1.2 shock with a water droplet in air at (a) $9 \mu\text{s}$, (b) $22 \mu\text{s}$, (c) $30 \mu\text{s}$, (d) $43 \mu\text{s}$, (e) $52 \mu\text{s}$, and (f) $174 \mu\text{s}$. The red contour line shows the material interface where $\alpha_D = 0.95$.

[Figs. 32(a)–32(c)]. As the refracted shock reaches the downstream interface, a weak rarefaction wave is internally reflected, and no significant shock is transmitted downstream [Figs. 32(d) and 32(e)].

-
- [1] M. Hersch, E. J. Rice, and Lewis Research Center, *Gaseous-Hydrogen-Liquid-Oxygen Rocket Combustion at Supercritical Chamber Pressures*, NASA Technical Note (NASA, Washington, DC, 1967).
 - [2] J. C. Oefelein, Thermophysical characteristics of shear-coaxial LOX–H₂ flames at supercritical pressure, *Proc. Combust. Inst.* **30**, 2929 (2005).
 - [3] D. T. Harrije and F. H. Reardon, *Liquid Propellant Rocket Combustion Instability* (Scientific and Technical Information Office, NASA, Washington, DC, 1972), Vol. 1.
 - [4] N. Okong', K. Harstad, and J. Bellan, Direct numerical simulations of O/H temporal mixing layers under supercritical conditions, *AIAA J.* **40**, 914 (2002).
 - [5] R. S. Miller, K. G. Harstad, and J. Bellan, Direct numerical simulations of supercritical fluid mixing layers applied to heptane-nitrogen, *J. Fluid Mech.* **436**, 1 (2001).
 - [6] R. Miller, K. Harstad, and J. Bellan, Evaluation of equilibrium and non-equilibrium evaporation models for many-droplet gas-liquid flow simulations, *Int. J. Multiphase Flow* **24**, 1025 (1998).
 - [7] J. Bellan, Supercritical (and subcritical) fluid behavior and modeling: Drops, streams, shear and mixing layers, jets and sprays, *Prog. Energy Combust. Sci.* **26**, 329 (2000).

- [8] W. O. H. Mayer, A. H. A. Schik, B. Vielle, C. Chauveau, I. Gokalp, D. G. Talley, and R. D. Woodward, Atomization and Breakup of Cryogenic Propellants Under High-Pressure Subcritical and Supercritical Conditions, *J. Propul. Power* **14**, 835 (1998).
- [9] N. Zong and V. Yang, Cryogenic fluid jets and mixing layers in transcritical and supercritical environments, *Combust. Sci. Technol.* **178**, 193 (2006).
- [10] B. Chehroudi, D. Talley, and E. Coy, Visual characteristics and initial growth rates of round cryogenic jets at subcritical and supercritical pressures, *Phys. Fluids* **14**, 850 (2002).
- [11] D. W. Davis, On the behavior of a shear-coaxial jet, spanning sub-to supercritical pressures, with and without an externally imposed transverse acoustic field, Ph.D. thesis, The Pennsylvania State University, 2006.
- [12] B. Chehroudi, Recent experimental efforts on high-pressure supercritical injection for liquid rockets and their implications, *Int. J. Aerosp. Eng.* **2012**, 121802 (2012).
- [13] I. Leyva, B. Chehroudi, and D. Talley, Dark core analysis of coaxial injectors at sub-, near-, and supercritical conditions in a transverse acoustic field, in *Proceedings of the 43rd AIAA/ASME/SAE/ASEE Joint Propulsion Conference and Exhibit*, 2007 (unpublished), p. 5456.
- [14] B. Chehroudi, Physical hypothesis for the combustion instability in cryogenic liquid rocket engines, *J. Propul. Power* **26**, 1153 (2010).
- [15] R. N. Dahms and J. C. Oefelein, On the transition between two-phase and single-phase interface dynamics in multicomponent fluids at supercritical pressures, *Phys. Fluids* **25**, 092103 (2013).
- [16] R. N. Dahms and J. C. Oefelein, Non-equilibrium gas-liquid interface dynamics in high-pressure liquid injection systems, *Proc. Combust. Inst.* **35**, 1587 (2015).
- [17] R. N. Dahms, J. Manin, L. M. Pickett, and J. C. Oefelein, Understanding high-pressure gas-liquid interface phenomena in Diesel engines, *Proc. Combust. Inst.* **34**, 1667 (2013).
- [18] R. N. Dahms, Understanding the breakdown of classic two-phase theory and spray atomization at engine-relevant conditions, *Phys. Fluids* **28**, 042108 (2016).
- [19] J. Oefelein, G. Lacaze, R. Dahms, A. Ruiz, and A. Misdariis, Effects of real-fluid thermodynamics on high-pressure fuel injection processes, *SAE Int. J. Engines* **7**, 1125 (2014).
- [20] R. N. Dahms and J. C. Oefelein, Liquid jet breakup regimes at supercritical pressures, *Combust. Flame* **162**, 3648 (2015).
- [21] C. Lettieri, G. Subashki, and Z. Spakovszky, Modeling near critical and supercritical fuel injection and mixing in gas turbine applications, in *ASME Turbo Expo (2018): Turbomachinery Technical Conference and Exposition* (American Society of Mechanical Engineers, New York, 2018), p. V04AT04A009.
- [22] Z. Ren, B. Wang, L. Zheng, and D. Zhao, Numerical studies on supersonic spray combustion in high-temperature shear flows in a scramjet combustor, *Chin. J. Aeronaut.* **31**, 1870 (2018).
- [23] Z. Ren, B. Wang, G. Xiang, D. Zhao, and L. Zheng, Supersonic spray combustion subject to scramjets: Progress and challenges, *Prog. Aerosp. Sci.* **105**, 40 (2019).
- [24] T.-M. Jia, Y.-S. Yu, and G.-X. Li, Experimental investigation of effects of super high injection pressure on diesel spray and induced shock waves characteristics, *Exp. Therm. Fluid Sci.* **85**, 399 (2017).
- [25] H. Chen, Two-dimensional simulation of stripping breakup of a water droplet, *AIAA J.* **46**, 1135 (2008).
- [26] H. Chen and S. M. Liang, Flow visualization of shock/water column interactions, *Shock Waves* **17**, 309 (2007).
- [27] B. Dorschner, L. Biasiori-Poulanges, K. Schmidmayer, H. El-Rabii, and T. Colonius, On the formation and recurrent shedding of ligaments in droplet aerobreakup, *J. Fluid Mech.* **904**, A20 (2020).
- [28] B. Guan, Y. Liu, C.-Y. Wen, and H. Shen, Numerical study on liquid droplet internal flow under shock impact, *AIAA J.* **56**, 3382 (2018).
- [29] D. Igra and K. Takayama, Numerical simulation of shock wave interaction with a water column, *Shock Waves* **11**, 219 (2001).
- [30] D. D. Joseph, J. Belanger, and G. S. Beavers, Breakup of a liquid drop suddenly exposed to a high-speed airstream, *Int. J. Multiphase Flow* **25**, 1263 (1999).
- [31] Y. Liang, Y. Jiang, C.-Y. Wen, and Y. Liu, Interaction of a planar shock wave and a water droplet embedded with a vapour cavity, *J. Fluid Mech.* **885**, R6 (2020).

- [32] J. C. Meng and T. Colonius, Numerical simulation of the aerobreakup of a water droplet, *J. Fluid Mech.* **835**, 1108 (2018).
- [33] J. C. Meng, Numerical simulations of droplet aerobreakup, Ph.D. thesis, California Institute of Technology, 2016.
- [34] B. Moylan, B. Landrum, and G. Russell, Investigation of the physical phenomena associated with rain impacts on supersonic and hypersonic flight vehicles, *Proc. Eng.* **58**, 223 (2013).
- [35] B. E. Moylan, Raindrop demise in a high-speed projectile flowfield, Ph.D. thesis, The University of Alabama in Huntsville, 2010.
- [36] Z. Wang, T. Hopfes, M. Giglmaier, and N. A. Adams, Effect of Mach number on droplet aerobreakup in shear stripping regime, *Exp. Fluids* **61**, 193 (2020).
- [37] T. Yoshida and K. Takayama, Interaction of liquid droplets with planar shock waves, *J. Fluids Eng.* **112**, 481 (1990).
- [38] J.-F. Haas and B. Sturtevant, Interaction of weak shock waves with cylindrical and spherical gas inhomogeneities, *J. Fluid Mech.* **181**, 41 (1987).
- [39] J. J. Quirk and S. Karni, On the dynamics of a shock-bubble interaction, *J. Fluid Mech.* **318**, 129 (2006).
- [40] S. Kumar, G. Orlicz, C. Tomkins, C. Goodenough, K. Prestridge, P. Vorobieff, and R. Benjamin, Stretching of material lines in shock-accelerated gaseous flows, *Phys. Fluids* **17**, 082107 (2005).
- [41] S. Kumar, P. Vorobieff, G. Orlicz, A. Palekar, C. Tomkins, C. Goodenough, M. Marr-Lyon, K. Prestridge, and R. Benjamin, Complex flow morphologies in shock-accelerated gaseous flows, *Physica D* **235**, 21 (2007).
- [42] G. Layes, G. Jourdan, and L. Houas, Distortion of a Spherical Gaseous Interface Accelerated by a Plane Shock Wave, *Phys. Rev. Lett.* **91**, 174502 (2003).
- [43] G. Layes, G. Jourdan, and L. Houas, Experimental investigation of the shock wave interaction with a spherical gas inhomogeneity, *Phys. Fluids* **17**, 028103 (2005).
- [44] G. Layes, G. Jourdan, and L. Houas, Experimental study on a plane shock wave accelerating a gas bubble, *Phys. Fluids* **21**, 074102 (2009).
- [45] K. Levy, O. Sadot, A. Rikanati, D. Kartoon, Y. Srebro, A. Yosef-Hai, G. Ben-Dor, and D. Shvarts, Scaling in the shock-bubble interaction, *Laser Part. Beams* **21**, 335 (2003).
- [46] J. H. J. Niederhaus, A computational parameter study for three-dimensional shock-bubble interactions, Ph.D. thesis, University of Wisconsin-Madison, 2007.
- [47] A. Nowakowski, A. Ballil, and F. Nicolleau, Passage of a shock wave through inhomogeneous media and its impact on gas-bubble deformation, *Phys. Rev. E* **92**, 023028 (2015).
- [48] D. Ranjan, J. Oakley, and R. Bonazza, Shock-bubble interactions, *Annu. Rev. Fluid Mech.* **43**, 117 (2011).
- [49] S. Sha, Z.-H. Chen, and Q.-B. Zhang, Numerical investigations on the interaction of shock waves with spherical SF₆ bubbles, *Acta Physica Sinica* **64**, 015201 (2015).
- [50] C. Tomkins, S. Kumar, G. Orlicz, and K. Prestridge, An experimental investigation of mixing mechanisms in shock-accelerated flow, *J. Fluid Mech.* **611**, 131 (2008).
- [51] C. Tomkins, K. Prestridge, P. Rightley, M. Marr-Lyon, P. Vorobieff, and R. Benjamin, A quantitative study of the interaction of two Richtmyer-Meshkov-unstable gas cylinders, *Phys. Fluids* **15**, 986 (2003).
- [52] Z.-G. Zhai, T. Si, L.-Y. Zou, and X.-S. Luo, Jet formation in shock-heavy gas bubble interaction, *Acta Mech. Sin.* **29**, 24 (2013).
- [53] Y. Zhu, Z. Yang, L. Gao, and K. H. Luo, Three-dimensional shock-sulfur hexafluoride bubble interaction, *AIP Adv.* **9**, 115306 (2019).
- [54] Y. Zhu, L. Yu, J. Pan, Z. Pan, and P. Zhang, Jet formation of SF₆ bubble induced by incident and reflected shock waves, *Phys. Fluids* **29**, 126105 (2017).
- [55] P. Waltrup, M. White, F. Zarlino, and E. Gravlin, History of US Navy ramjet, scramjet, and mixed-cycle propulsion development, *J. Propul. Power* **18**, 14 (2002).
- [56] M. L. Fotia, Mechanics of combustion mode transition in a direct-connect ramjet–scramjet experiment, *J. Propul. Power* **31**, 69 (2015).

- [57] D. Banuti, M. Raju, P. C. Ma, M. Ihme, and J.-P. Hickey, Seven questions about supercritical fluids-towards a new fluid state diagram, in *Proceedings of the 55th AIAA Aerospace Sciences Meeting*, 2017 (unpublished), p. 1106.
- [58] M. Raju, D. T. Banuti, P. C. Ma, and M. Ihme, Widom lines in binary mixtures of supercritical fluids, *Sci. Rep.* **7**, 3027 (2017).
- [59] J. W. Chae, H. S. Yang, and W. S. Yoon, Supercritical droplet dynamics and emission in low speed cross-flows, *J. Mech. Sci. Technol.* **22**, 1586 (2008).
- [60] V. Yang, Modeling of supercritical vaporization, mixing, and combustion processes in liquid-fueled propulsion systems, *Proc. Combust. Inst.* **28**, 925 (2000).
- [61] V. Yang, N. N., and J.-S. Shuen, Vaporization of liquid oxygen (LOX) droplets in supercritical hydrogen environments, *Combust. Sci. Technol.* **97**, 247 (1994).
- [62] K.-C. Hsieh, Droplet behavior at supercritical conditions, *Recent Adv. Spray Combust.: Spray Atom. Drop Burn. Phenom.* **1**, 413 (1996).
- [63] C. Crua, J. Manin, and L. M. Pickett, On the transcritical mixing of fuels at diesel engine conditions, *Fuel* **208**, 535 (2017).
- [64] H. Meng, G. C. Hsiao, V. Yang, and J. S. Shuen, Transport and dynamics of liquid oxygen droplets in supercritical hydrogen streams, *J. Fluid Mech.* **527**, 115 (2005).
- [65] P. Das and H. S. Udaykumar, A sharp-interface method for the simulation of shock-induced vaporization of droplets, *J. Comput. Phys.* **405**, 109005 (2020).
- [66] H. J. Q. Wan, R. Deiterding, and V. Eliasson, Numerical and experimental investigation of oblique shock wave refraction of a water wedge, *J. Fluid Mech.* **826**, 732 (2017).
- [67] D. P. Garrick, M. Owkes, and J. D. Regele, A finite-volume HLLC-based scheme for compressible interfacial flows with surface tension, *J. Comput. Phys.* **339**, 46 (2017).
- [68] J. C. Meng and T. Colonius, Numerical simulations of the early stages of high-speed droplet breakup, *Shock Waves* **25**, 399 (2014).
- [69] D. P. Garrick, W. A. Hagen, and J. D. Regele, An interface capturing scheme for modeling atomization in compressible flows, *J. Comput. Phys.* **344**, 260 (2017).
- [70] P. Tudisco and S. Menon, Numerical investigations of phase-separation during multi-component mixing at super-critical conditions, *Flow, Turbul. Combust.* **104**, 693 (2020).
- [71] B. Boyd and D. Jarrahbashi, A diffuse-interface method for reducing spurious pressure oscillations in multicomponent transcritical flow simulations, *Comput. Fluids* **222**, 104924 (2021).
- [72] R. Abgrall, How to prevent pressure oscillations in multicomponent flow calculations: A quasi conservative approach, *J. Comput. Phys.* **125**, 150 (1996).
- [73] P. C. Ma, Y. Lv, and M. Ihme, An entropy-stable hybrid scheme for simulations of transcritical real-fluid flows, *J. Comput. Phys.* **340**, 330 (2017).
- [74] P. C. Ma, H. Wu, T. Jaravel, L. Bravo, and M. Ihme, Large-eddy simulations of transcritical injection and auto-ignition using diffuse-interface method and finite-rate chemistry, *Proc. Combust. Inst.* **37**, 3303 (2019).
- [75] J. Matheis and S. Hickel, Multi-component vapor-liquid equilibrium model for LES of high-pressure fuel injection and application to ECN Spray A, *Int. J. Multiphase Flow* **99**, 294 (2018).
- [76] A. M. Ruiz, G. Lacaze, J. C. Oefelein, R. Mari, B. Cuenot, L. Selle, and T. Poinsot, Numerical benchmark for high-Reynolds-number supercritical flows with large density gradients, *AIAA J.* **54**, 1445 (2016).
- [77] T. Schmitt, L. Selle, A. Ruiz, and B. Cuenot, Large-eddy simulation of supercritical-pressure round jets, *AIAA J.* **48**, 2133 (2010).
- [78] H. Müller, C. A. Niedermeier, J. Matheis, M. Pfizner, and S. Hickel, Large-eddy simulation of nitrogen injection at trans-and supercritical conditions, *Phys. Fluids* **28**, 015102 (2016).
- [79] J. Oefelein, R. Dahms, and G. Lacaze, Detailed modeling and simulation of high-pressure fuel injection processes in diesel engines, *SAE Int. J. Engines* **5**, 1410 (2012).
- [80] W. Wei, H. Liu, M. Xie, M. Jia, and M. Yue, Large eddy simulation and proper orthogonal decomposition analysis of fuel injection under trans/supercritical conditions, *Comput. Fluids* **179**, 150 (2019).

- [81] D. T. Banuti, P. C. Ma, and M. Ihme, Phase separation analysis in supercritical injection using large-eddy-simulation and vapor-liquid-equilibrium, in *Proceedings of the 53rd AIAA/SAE/ASEE Joint Propulsion Conference*, 2017 (unpublished), p. 4764.
- [82] N. Okong'o and J. Bellan, Perturbation and initial Reynolds number effects on transition attainment of supercritical, binary, temporal mixing layers, *Comput. Fluids* **33**, 1023 (2004).
- [83] N. Okong'o and J. Bellan, Small-scale dissipation in binary-species, thermodynamically supercritical, transitional mixing layers, *Comput. Fluids* **39**, 1112 (2010).
- [84] D. T. Banuti, M. Raju, and M. Ihme, Supercritical pseudoboiling for general fluids and its application to injection, *Annual Research Briefs*, 211 (2016).
- [85] M. Oschwald, J. Smith, R. Branam, J. Hussong, A. Schik, B. Chehroudi, and D. Talley, Injection of fluids into supercritical environments, *Combust. Sci. Technol.* **178**, 49 (2006).
- [86] D.-Y. Peng and D. B. Robinson, A new two-constant equation of state, *Indust. Eng. Chem. Fundam.* **15**, 59 (1976).
- [87] B. J. McBride, *Coefficients for Calculating Thermodynamic and Transport Properties of Individual Species* (NASA Langley Research Center, Washington, DC, 1993), Vol. 4513.
- [88] P. C. Ma, H. Wu, D. T. Banuti, and M. Ihme, On the numerical behavior of diffuse-interface methods for transcritical real-fluids simulations, *Int. J. Multiphase Flow* **113**, 231 (2019).
- [89] E. Johnsen and T. Colonius, Implementation of WENO schemes in compressible multicomponent flow problems, *J. Comput. Phys.* **219**, 715 (2006).
- [90] V. Coralic and T. Colonius, Finite-volume WENO scheme for viscous compressible multicomponent flows, *J. Comput. Phys.* **274**, 95 (2014).
- [91] A. Harten, B. Engquist, S. Osher, and S. R. Chakravarthy, Uniformly high order accurate essentially non-oscillatory schemes, III, *J. Comput. Phys.* **131**, 3 (1997).
- [92] J. Qiu and C.-W. Shu, On the construction, comparison, and local characteristic decomposition for high-order central WENO schemes, *J. Comput. Phys.* **183**, 187 (2002).
- [93] S. Gottlieb and C.-W. Shu, Total variation diminishing Runge-Kutta schemes, *Math. Comput.* **67**, 73 (1998).
- [94] B. Boyd and S. Becker, Numerical modelling of an acoustically-driven bubble collapse near a solid boundary, *Fluid Dyn. Res.* **50**, 065506 (2018).
- [95] B. Boyd and S. Becker, Numerical modeling of the acoustically driven growth and collapse of a cavitation bubble near a wall, *Phys. Fluids* **31**, 032102 (2019).
- [96] X. Zhang and C.-W. Shu, Maximum-principle-satisfying and positivity-preserving high-order schemes for conservation laws: Survey and new developments, *Proc. R. Soc. A* **467**, 2752 (2011).
- [97] B. Boyd, Numerical modelling of an acoustically-driven bubble: The growth and collapse near a wall, Ph.D. thesis, University of Canterbury, 2018.
- [98] R. P. Fedkiw, T. Aslam, B. Merriman, and S. Osher, A non-oscillatory Eulerian approach to interfaces in multimaterial flows (the ghost fluid method), *J. Comput. Phys.* **152**, 457 (1999).
- [99] B. Hejzalianhosseini, D. Rossinelli, M. Bergdorf, and P. Koumoutsakos, High order finite volume methods on wavelet-adapted grids with local time-stepping on multicore architectures for the simulation of shock-bubble interactions, *J. Comput. Phys.* **229**, 8364 (2010).
- [100] X. Y. Hu and B. C. Khoo, An interface interaction method for compressible multifluids, *J. Comput. Phys.* **198**, 35 (2004).
- [101] W. Liu, L. Yuan, and C.-W. Shu, A conservative modification to the ghost fluid method for compressible multiphase flows, *Commun. Comput. Phys.* **10**, 785 (2015).
- [102] A. Marquina and P. Mulet, A flux-split algorithm applied to conservative models for multicomponent compressible flows, *J. Comput. Phys.* **185**, 120 (2003).
- [103] R. K. Shukla, C. Pantano, and J. B. Freund, An interface capturing method for the simulation of multiphase compressible flows, *J. Comput. Phys.* **229**, 7411 (2010).
- [104] K. K. So, X. Y. Hu, and N. A. Adams, Anti-diffusion interface sharpening technique for two-phase compressible flow simulations, *J. Comput. Phys.* **231**, 4304 (2012).
- [105] H. Terashima and G. Tryggvason, A front-tracking/ghost-fluid method for fluid interfaces in compressible flows, *J. Comput. Phys.* **228**, 4012 (2009).

- [106] L. Wang, G. M. D. Currao, F. Han, A. J. Neely, J. Young, and F.-B. Tian, An immersed boundary method for fluid–structure interaction with compressible multiphase flows, *J. Comput. Phys.* **346**, 131 (2017).
- [107] D. Ranjan, J. H. Niederhaus, J. G. Oakley, M. H. Anderson, R. Bonazza, and J. A. Greenough, Shock-bubble interactions: Features of divergent shock-refraction geometry observed in experiments and simulations, *Phys. Fluids* **20**, 036101 (2008).
- [108] K. Narayanaswamy, P. Pepiot, and H. Pitsch, A chemical mechanism for low to high temperature oxidation of *n*-dodecane as a component of transportation fuel surrogates, *Combust. Flame* **161**, 866 (2014).
- [109] D. R. Guildenbecher, C. López-Rivera, and P. E. Sojka, Secondary atomization, *Exp. Fluids* **46**, 371 (2009).
- [110] E. Meshkov, Instability of the interface of two gases accelerated by a shock wave, *Fluid Dyn.* **4**, 101 (1969).
- [111] R. D. Richtmyer, Taylor instability in shock acceleration of compressible fluids, Los Alamos Scientific Lab., N. Mex (1954), <https://www.osti.gov/biblio/4272289>.
- [112] T. G. Theofanous and G. J. Li, On the physics of aerobreakup, *Phys. Fluids* **20**, 052103 (2008).
- [113] G. C. Orlicz, S. Balasubramanian, and K. P. Prestridge, Incident shock Mach number effects on Richtmyer-Meshkov mixing in a heavy gas layer, *Phys. Fluids* **25**, 114101 (2013).
- [114] A. R. Staff, Equations, tables, and charts for compressible flow, NACA Report No. 1135, 1953 (unpublished).
- [115] C.-H. Chang and M.-S. Liou, A robust and accurate approach to computing compressible multiphase flow: Stratified flow model and AUSM+-up scheme, *J. Comput. Phys.* **225**, 840 (2007).
- [116] A. Wierzba and K. Takayama, Experimental investigation of the aerodynamic breakup of liquid drops, *AIAA J.* **26**, 1329 (1988).
- [117] G. Allaire, S. Clerc, and S. Kokh, A five-equation model for the simulation of interfaces between compressible fluids, *J. Comput. Phys.* **181**, 577 (2002).